



# Centrifuge and numerical modeling of the behavior of homogeneous embankment on liquefiable soil subjected to dynamic excitation

Chedid Saade, Zheng Li, Sandra Escoffier, Luc Thorel

## ► To cite this version:

Chedid Saade, Zheng Li, Sandra Escoffier, Luc Thorel. Centrifuge and numerical modeling of the behavior of homogeneous embankment on liquefiable soil subjected to dynamic excitation. *Soil Dynamics and Earthquake Engineering*, 2023, 172, pp.107999. 10.1016/j.soildyn.2023.107999 . hal-04272728

**HAL Id: hal-04272728**

**<https://univ-eiffel.hal.science/hal-04272728>**

Submitted on 6 Nov 2023

**HAL** is a multi-disciplinary open access archive for the deposit and dissemination of scientific research documents, whether they are published or not. The documents may come from teaching and research institutions in France or abroad, or from public or private research centers.

L'archive ouverte pluridisciplinaire **HAL**, est destinée au dépôt et à la diffusion de documents scientifiques de niveau recherche, publiés ou non, émanant des établissements d'enseignement et de recherche français ou étrangers, des laboratoires publics ou privés.

# Centrifuge and numerical modeling of the behavior of homogeneous embankment on liquefiable soil subjected to dynamic excitation

Chedid SAADE\*, Zheng LI, Sandra ESCOFFIER, Luc THOREL

*Laboratoire Centrifugeuses Géotechniques (CG), Département Géotechnique, Environnement, Risques Naturels et Science de la Terre (GERS),  
Université Gustave Eiffel  
Allée des Ponts et Chaussées, CS 5004, 44344, Bouguenais, France*

---

## Abstract

Centrifuge and numerical modeling are developed to investigate the behavior of a homogeneous embankment constructed on a liquefiable sand ground, which was prepared with wet under-compaction method. The physical centrifuge modeling directly highlights the response of the centrifuge model in terms of excess pore pressure, acceleration response, settlement, and the deformation pattern of the embankment model. In parallel, a numerical simulation using FEM is conducted. The advanced constitutive model, PM4Sand, is adopted to simulate the liquefaction of the sand ground. The performance of the numerical model is then verified against the results of the centrifuge test. Overall, the numerical simulation aligns well with the centrifuge test. Finally, the verified numerical model is refined to include two improved boundaries, and the potential boundary effects in centrifuge and numerical models are discussed.

**Keywords:** Centrifuge modeling; Numerical modeling; Embankment; Ground liquefaction

---

## List of symbols

$CRR$ Cyclic resistance ratio	$t_2$ Start time of decreasing stage of permeability
$CRR_{TX}$ Cyclic resistance ratio of cyclic triaxial test	$t_3$ End time of decreasing stage of permeability
$D_{50}$ Mean particle diameter	$G_{max}$ Maximum shear modulus
$e$ Void ratio	$G_o$ Shear modulus coefficient
$e_{max}$ Maximum void ratio	$G_s$ Specific gravity
$e_{min}$ Minimum Void ratio	$g$ Earth gravity
$t$ Time	$h_{po}$ Contraction rate parameter

---

\*Corresponding author

Email addresses: chedid.saade@univ-eiffel.fr (Chedid SAADE ), zheng.li@univ-eiffel.fr (Zheng LI), sandra.escoffier@univ-eiffel.fr (Sandra ESCOFFIER), luc.thorel@univ-eiffel.fr (Luc THOREL)



$h_o$	Secondary input parameter that adjusts the ratio of plastic modulus to elastic modulus	$V_s$	Shear wave velocity
$I_D$	Relative density	$X$	Horizontal position
$k$	Permeability	$Y$	Vertical position
$k_i$	Initial permeability	$\alpha$	Constant controls the variation of excess pore pressure
$k_b$	Permeability in excess pore pressure build up stage	$\alpha_2$	Constant controls the variation of excess pore pressure
$k_d$	Permeability in excess pore pressure decreasing stage	$\beta_1$	Constant controls the variation of excess pore pressure
$k_l$	Permeability in liquefaction stage	$\beta_2$	Constant controls the variation of excess pore pressure
$K_0$	Lateral earth pressure coefficient	$\Delta u$	Excess pore pressure
$N$	Number of cycles required for liquefaction	$\nu$	Poisson's ratio
$p_A$	Atmospheric pressure	$\rho_{sat}$	Saturated density of the soil
$p'$	Mean effective stress	$\rho_{dmin}$	Minimum dry density
$p_e$	Experimental value	$\rho_{dmax}$	Maximum dry density
$p_n$	Numerical value	$\sigma_v$	Initial vertical stress
$Q$	Bolton's constant in PM4Sand model	$\sigma'_v$	Initial vertical effective stress
$R$	Bolton's constant in PM4Sand model	$\phi$	Critical state friction angle
$r_u$	Excess pore water pressure ratio		
$S$	Anderson's score		

## 1. Introduction

Earth dams, levees, berms, and embankments have played an important role in the development of infrastructure throughout history. Considered among the oldest forms of construction in civil engineering, these structures serve multiple purposes, including transportation, irrigation, flood control, and power generation. Their failure may cause a huge disaster and loss of lives and facilities (Wu *et al.*, 2012). Under dynamic loading, dam failures like cracks, huge settlements or internal erosion can occur (Veylon, 2017) even in low to medium seismic zones (Kawakami and Asada, 1966; Seed *et al.*, 1980). Historical cases, for example the Chilean earthquake in 1960 (Duke, 1960), the

San Fernando Earthquake in 1971 (Seed *et al.*, 1975) and the Tohoku earthquake in 2011 (Yamaguchi *et al.*, 2012; Oka *et al.*, 2012), reveal that earthquake-induced liquefaction was the most significant cause of embankment failure. Therefore, the study of the damage or even failure of embankment due to the earthquake-induced liquefaction is of considerable importance from both public safety and financial standpoints.

In recent decades, physical tests have been conducted to directly observe and study the behavior and failure mechanisms of embankments under dynamic loading. Shaking table tests have been utilized to investigate the embankment response to soil ground liquefaction. For instance, studies by Iwasaki (1986), Koga and Matsuo (1990) and Park *et al.* (2000) have reported significant deformations in the embankment, including crest settlement and lateral displacement of embankment sides. Besides the 1g shaking table tests, Ng centrifuge modeling could be regarded as a better option in the study of embankment failure due to liquefaction. Based on the theory of scaling laws and the principle of stress similitude (Garnier *et al.*, 2007), centrifuge modeling allows to interpret the behavior of a large-scale prototype model with a reduced-size model that subjected to the artificial macro-gravity. Many centrifuge tests in the literature (e.g. Ng *et al.* (2004), Okamura *et al.* (2013), Higo *et al.* (2015), Adapa *et al.* (2021) and Izawa *et al.* (2022)) have focused on the responses of embankments resting on non-liquefiable ground under earthquakes actions. Centrifuge tests were conducted by Adalier and Sharp (2004), Pramaditya and Fathani (2021a) and Pourakbar *et al.* (2022) to investigate the response of the embankment to soil ground liquefaction. These studies found that liquefaction typically occurs beneath the ground surface near the toe of the embankment, while the soil beneath the embankment is less susceptible to liquefaction. Furthermore, Adalier *et al.* (1998) investigated the effects of the thickness and position of the liquefiable layer on embankment behavior. Additionally, Park *et al.* (2000), Okamura and Matsuo (2002), Tiznado *et al.* (2020), Li *et al.* (2021), Pramaditya and Fathani (2021b) and Pourakbar *et al.* (2022) have highlighted the effects of liquefaction remediation on embankment response, taking into account different types of liquefaction reinforcement.

Numerical modeling or simulation is a versatile and important technical approach that has been utilized in the geotechnical earthquake engineering community to study soil liquefaction. The numerical simulations of earthquake-induced liquefaction were mainly conducted on the continuum domain by exploiting either Finite Element Method (FEM) (Finn, 1999; Elgamal *et al.*, 2002; Aydingun and Adalier, 2003; Okochi *et al.*, 2015; Bhatnagar *et al.*, 2016; Gobbi *et al.*, 2017; Rapti *et al.*, 2018; Chakraborty and Sawant, 2022) or Finite Difference Method (FDM) (Wu *et al.*, 2009; Bouraoui and Benmebarek, 2018; Ziotopoulou, 2018; Boulanger *et al.*, 2015; Boulanger and Montgomery, 2016; Dinesh *et al.*, 2022). The main objectives of these numerical simulations were to predict the behavior or the failure of the embankment due to earthquake-induced liquefaction.

In order to have a more accurate and realistic prediction of the complex liquefaction phenomena, in the literature, many constitutive models were proposed and then used in the simulation of liquefaction-related problems. Examples of the constitutive models for liquefaction analysis include the multi-surface plasticity model (Elgamal *et al.*, 2003), the bounding surface plasticity model – SANISAND (Dafalias and Manzari, 2004), the UBCSand model (Beaty and Byrne, 2011), the coupled effective stress WANG model (Wang and Ma, 2019) *etc.* Recently, Dinesh *et al.* (2022) used an advanced constitutive model PM4Sand implemented in FLAC 2D to simulate the same centrifuge

test. It has been shown that the numerical model with PM4Sand constitutive law was able to reproduce correctly the responses in terms of accelerations and excess pore pressures. In recent years, the PM4Sand constitutive model has proven to be successful in simulating soil liquefaction (Rahmani *et al.*, 2012; Chiaradonna *et al.*, 2022) and in investigating its effect on the behavior of various geotechnical structures, such as dams (Boulanger and Ziotopoulou, 2015; Boulanger and Montgomery, 2016; Lu *et al.*, 2022), traffic embankments (Oblak *et al.*, 2020), structures with shallow foundation (Kassas *et al.*, 2021b) and offshore pipelines (Seth *et al.*, 2022). PM4Sand is also one of the recommended models by United States Society on Dams (USSD) for the seismic analysis of embankments, dams, and levees (USSD, 2022).

This study investigates the behavior of a homogeneous embankment on liquefiable sand ground under dynamic loading, using a combined experimental and numerical approach. The liquefiable ground was constructed with the wet under-compaction method and the effect of the humid tamping on the liquefaction resistance of sand was carefully considered. Although a rigid (or strong) container without any additional absorbing materials was used in the centrifuge test, the impact of boundary effects was found to be limited. The outline of this paper is as follows. Firstly, the experimental set-up including the model geometry, model preparation and instrumentation is presented. Then, the numerical modeling of the centrifuge test is discussed in detail, including FEM mesh, boundary conditions, constitutive model calibration, and modeling execution procedure *etc.* Next, the experimental results in terms of the model responses and liquefaction pattern are presented and discussed. The performance of the numerical model is then verified by comparing the experimental and numerical results in terms of acceleration, excess pore pressure, model deformation pattern, settlement *etc.* Finally, the effects of the boundary conditions on the model responses are evaluated numerically with models with larger and different boundaries.

## 2. Experimental set-up of the dynamic centrifuge test

In the present study, the dynamic centrifuge test was conducted at the University Gustave Eiffel (Nantes Campus). The centrifugal acceleration level was 60 g. To excite the model, a 1D shaking table embedded in the swinging basket was employed, as previously described by Chazelas *et al.* (2008). This section provides a detailed description of the experimental set-up utilized in the dynamic centrifuge test.

### 2.1. Geometry and dimensions of the centrifuge model

The geometry of the centrifuge model is shown in Fig. 1. According to the scaling laws (Garnier *et al.*, 2007), the reduced-size centrifuge model represents a prototype embankment of 6 m in height, which rests on a liquefiable layer 9 m thick. The slope of the embankment is determined to be 1/1.5, which is closed to the friction angle of the sand that was used in the embankment of the centrifuge model.

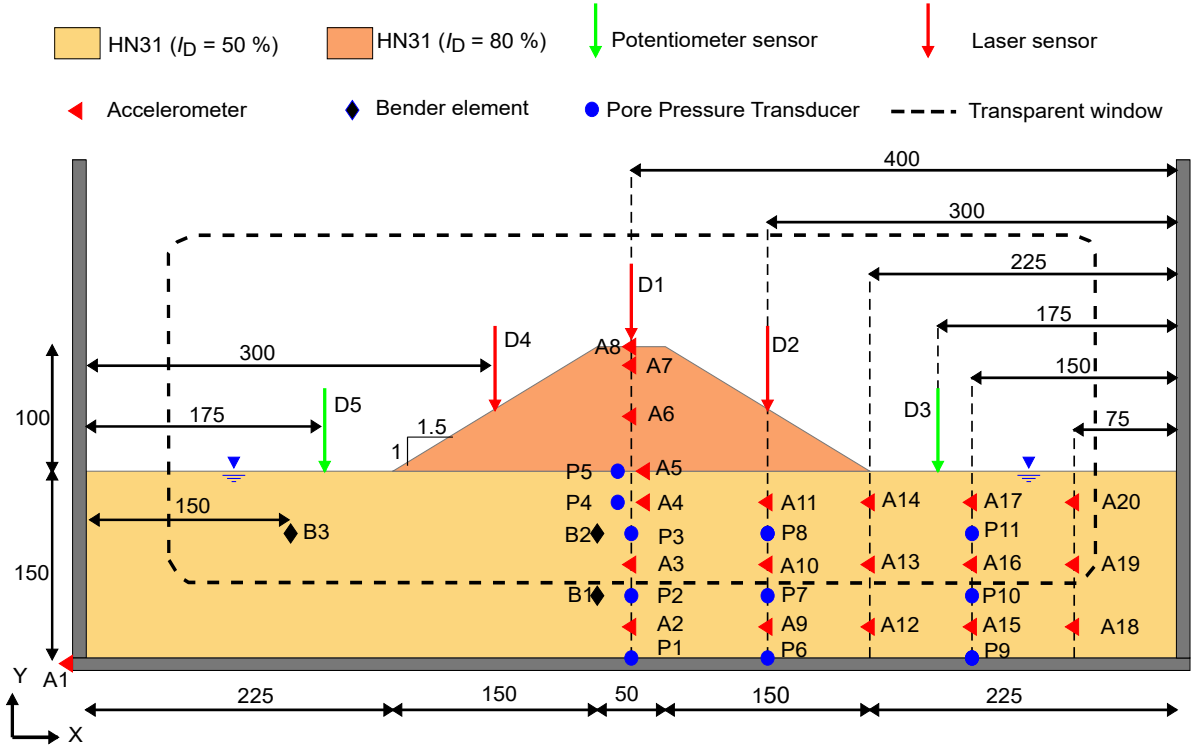


Figure 1: Centrifuge model at model scale,  $N=1/60$  (Dimensions in mm)

## 2.2. Materials of the centrifuge model

The sand used to reconstitute the ground and the embankment was Hostun HN31 sand. Hostun HN31 sand is a fine sub-angular to angular siliceous sand (Benahmed, 2001; Benahmed *et al.*, 2004) and its main properties are listed in Table 1. The ground layer is fully saturated with a fluid that has a viscosity 60 times (60 cSt) higher than pure water to satisfy the scaling laws in the centrifuge test at 60g (Adamidis and Madabhushi, 2015). The viscous fluid was prepared by a mixture of water with hydroxypropyl methylcellulose (HPMC) (Dewoolkar *et al.*, 1999; Escoffier and Audrain, 2020).

Table 1: Properties of Hostun sand HN31 (Benahmed, 2001; Benahmed *et al.*, 2004)

Sand	$D_{50}$ (mm)	$e_{\min}$	$e_{\max}$	$G_s$	$\rho_{\min}$ (g/cm <sup>3</sup> )	$\rho_{\max}$ (g/cm <sup>3</sup> )
Hostun HN31	0.35	0.656	1.049	2.65	1.33	1.6

## 2.3. Soil container

The model was built in a rigid container (see Fig 2) which has the inner dimensions of 800 mm (length)  $\times$  400 mm (height)  $\times$  340 mm (width). The soil container has a transparent on one side that allows the direct observation by cameras during the test. Doubled-face tapes were attached at the bottom of the container to enhance interface friction and ensure good transmission of the shear waves in the sand.

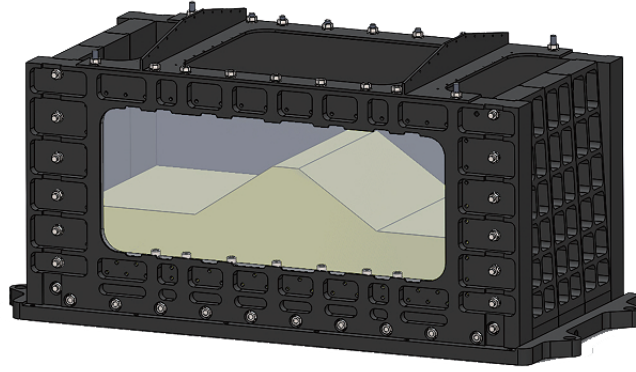


Figure 2: Illustration of the rigid container

## 2.4. Model preparation

The centrifuge model was prepared in two different steps. The ground layer and the embankment were prepared by different techniques proposed by [Adalier and Sharp \(2004\)](#). In this section, a detailed procedure for preparing the soil ground and the embankment is presented.

### 2.4.1. Liquefiable ground layer

The liquefiable ground layer which had a total thickness of 150 mm was prepared by the under-compaction method proposed by [Ladd \(1974\)](#). The moist Hostun HN31 sand was used with a 5% content of viscous fluid for tamping. The ground soil was then compacted layer by layer using a rectangular tamper of 1.4 kg which was dropped from a fixed height of 70 mm. As the tamper completed one compact at each position, it moved on to the next, until the height of the soil layer reached the controlled under-compaction depth. The levelness of each soil layer after under-compaction was carefully checked. Totally, six layers of sand were prepared for the ground layer. The relative density  $I_D$  was controlled at around  $50.0\% \pm 2\%$ .

### 2.4.2. Embankment

After completing the ground layer, a flat layer of dry dense Hostun HN31 sand with a thickness of 100 mm was then prepared using air pluviation. The pluviation was carried out with an automatic sand hopper ([Garnier, 2001](#)) with a slot opening equal to 4 mm, a falling height of 750 mm and a constant horizontal moving speed of 100 mm/s. With these parameters, the relative density  $I_D$  was estimated around  $80.0\% \pm 1.5\%$ . In order to achieve the desired shape without disturbing the dry sand of the embankment, the flat layer of dry sand was carefully and gradually trimmed using a vacuum cleaner (Fig. 3). Finally, the shape of the embankment was double-checked with a wooden mould.

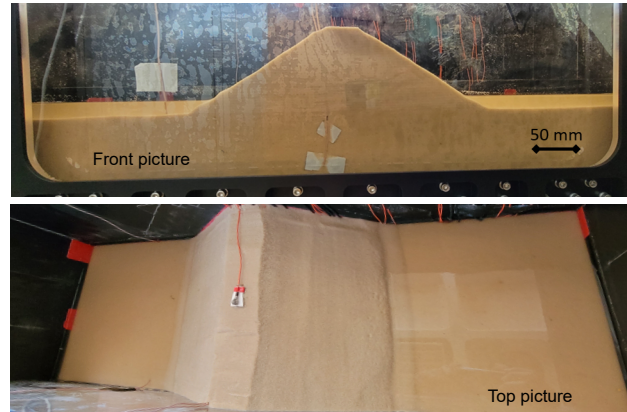


Figure 3: Final shape of the instrumented centrifuge model

#### 2.4.3. Model saturation

The centrifuge model was saturated with viscous fluid at 1g in a vacuum chamber following the saturation procedure proposed by Ueno (1998) and Mulilis (1975). The air in the model was removed by applying vacuum and then flushing CO<sub>2</sub> by two times. Then, viscous fluid was injected into the centrifuge model under an absolute pressure of 50 mbar from the bottom of the container. After the saturation process was completed and the water level reached 5 mm above ground surface, the degree of saturation of the ground layer was checked by using the “laser-floater” method proposed by Okamura and Inoue (2012). The global degree of saturation was estimated to be approximately 99.0%.

#### 2.5. Instrumentation

The type and location of the sensors are shown in Fig. 1 and the detailed information about the sensors is listed in Table 2. Totally, 20 accelerometers (A) and 11 pore pressures transducers (P) were installed to follow the soil motion and the pore pressure evolution during the dynamic event, respectively. For example, Fig. 4 illustrates the positioning of a 1D accelerometer at a certain depth in the sand. There were also three pairs of bender element located at three different depths. Three laser displacement sensors were installed to track the settlements of the crest and mid-slope of the embankment. Two potentiometer sensors were also placed at the free ground surface near the toe of the embankment.

Table 2: Instrumentation of the centrifuge model

Sensor type	Sensor notation	Working range	Manufacturing precision (%)	Number
Accelerometer	A	1 Hz-20 kHz	0.3 %	20
Pore pressure transducer	P	0-2 bars	0.2 %	11
Laser displacement	D (in red)	16-120 mm	0.1 %	3
Potentiometer	D (in green)	0-100 mm	0.1 %	2

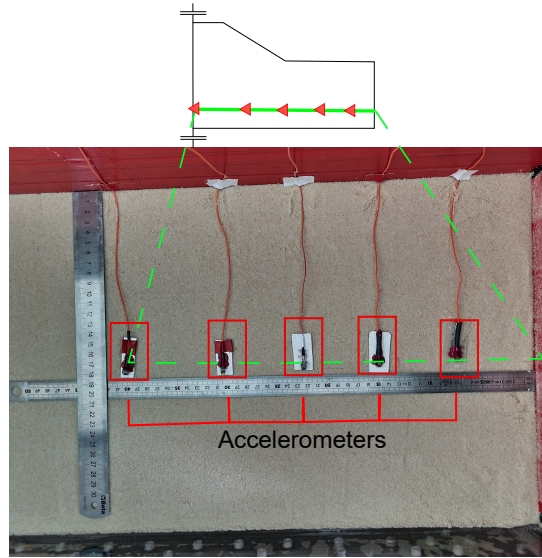


Figure 4: Centrifuge model in preparation - installation of accelerometers

## 2.6. Experimental program

The dynamic centrifuge test was performed in three stages: in-flight consolidation, bender element test and shaking/excitation. For the in-flight consolidation, the centrifuge model was gradually spun up 10 g by 10 g until up to 60 g. The model was then kept at 60 g for 10 mins to fully consolidate the model in  $K_0$  condition and stabilize the initial geo-static stress and pore pressures. Fig. 5 shows the initial pore pressure profiles obtained from the theoretical calculation, FEM solution (its details were introduced in Section 3 hereafter.) and experimental measurement. The pore pressure profiles were also compared under the embankment and under the free ground. The experimental measurement agreed well with the numerical model and the theoretical calculation. The theoretical profile was calculated by assuming an absolute dry state of the embankment, with the water level exactly at the surface of the ground. However, during the centrifuge test, the embankment was in an unsaturated state (with an estimated fluid content of around 3.5%). At the interface between the embankment and ground, the actual water level in the center of the embankment was slightly higher than that of the ground surface. This effect was observed in the numerical model and experimental measurement after consolidation, as it is shown in Fig. 5.

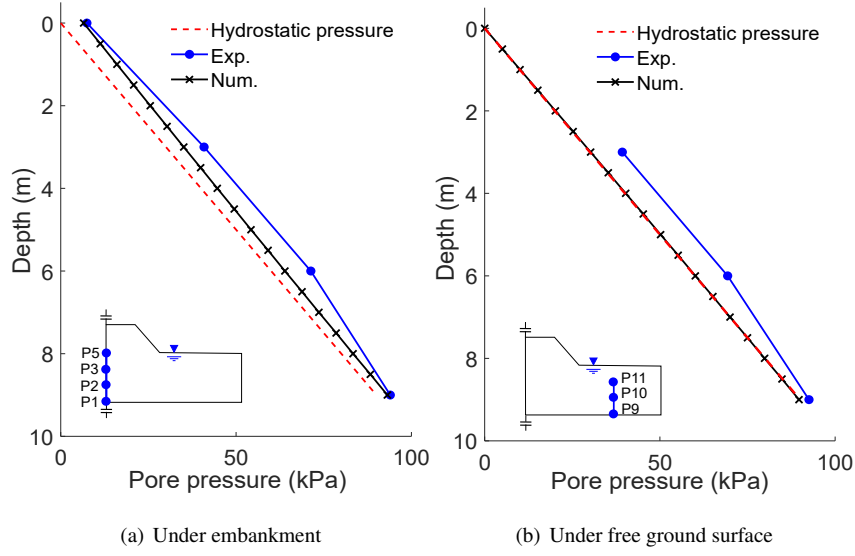


Figure 5: Comparison of initial static pore pressures of the centrifuge and numerical model after consolidation with the theoretical hydrostatic pressures: (a) under the embankment and (b) under the free ground surface

After in-flight consolidation and before the shaking, bender element tests were performed to measure the shear wave velocities at three different depths, see Fig. 1. Then, the model was subjected to a 1D horizontal sinusoidal base shaking. As it is shown in Fig. 6, the target input signal used in the test consisted of 20 full cycles with a dominant frequency of 1.5 Hz and an amplitude of 0.2 g in prototype scale. Due to the non-perfect response of the hydraulic shaker, the input signal was unavoidably noised by multiple high-frequency contents with small amplitudes. Fig. 6 also shows the actual input signal and its frequency contents measured at the base of the container (A1). As a result of the presence of these small amplitudes at higher frequencies, the peak acceleration of the actual input signal is therefore slightly higher than that of the target amplitude.

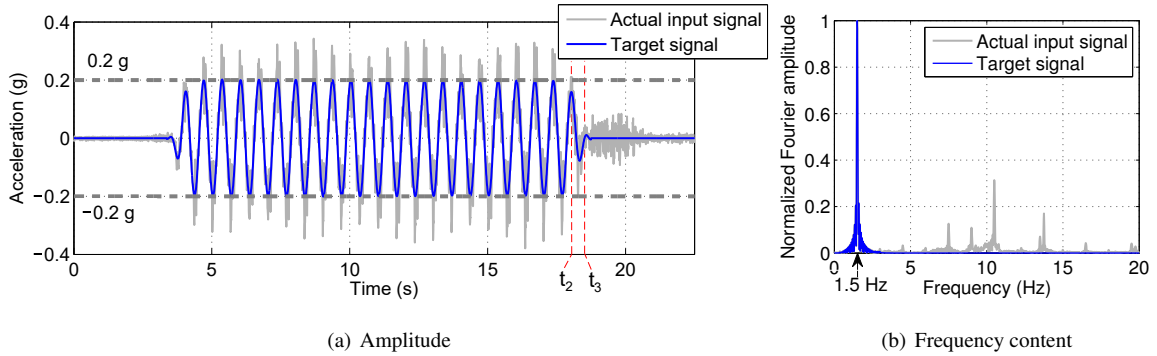


Figure 6: Time and frequency representations of the input signal (target and actual) in prototype scale (a) amplitude and (b) normalized frequency content



### 3. Numerical modeling

The numerical simulation of the centrifuge test was carried out on the OpenSees platform – “*Open System for Earthquake Engineering Simulation*”, which is a well known finite element method based open source code (McKenna *et al.*, 2006). In this section, a detailed description is provided regarding the FEM mesh, boundary conditions, constitutive laws, and calibration of the constitutive model parameters.

#### 3.1. FEM mesh and boundary conditions

The numerical model was built at the prototype scale and the FEM mesh is shown in Fig. 7. The ground soil and embankment were modeled using 4-node quadrilateral SSPquadUP elements. The SSPquadUP element which has a mixed displacement-pressure  $u - p$  formulation enables the dynamic plane strain analysis of fluid saturated porous media (McGann *et al.*, 2012). There were 1728 elements and 756 elements for the soil ground and the embankment, respectively. According to the mesh sensitivity analyses, the results of the model with the current mesh density (mesh size  $\approx 0.5$  m) are accurate enough.

The boundary conditions in the numerical model were chosen to accurately reflect the actual conditions in the rigid container which was used in the dynamic centrifuge test. All the nodes at the base were fixed in both horizontal  $X$  and vertical  $Y$  directions. While the lateral sides of the model were fixed only in the horizontal  $X$  direction. Drained conditions were assigned to the surfaces of the ground and the embankment (blue dashed line); while undrained conditions were assigned to the bottom and the lateral sides.

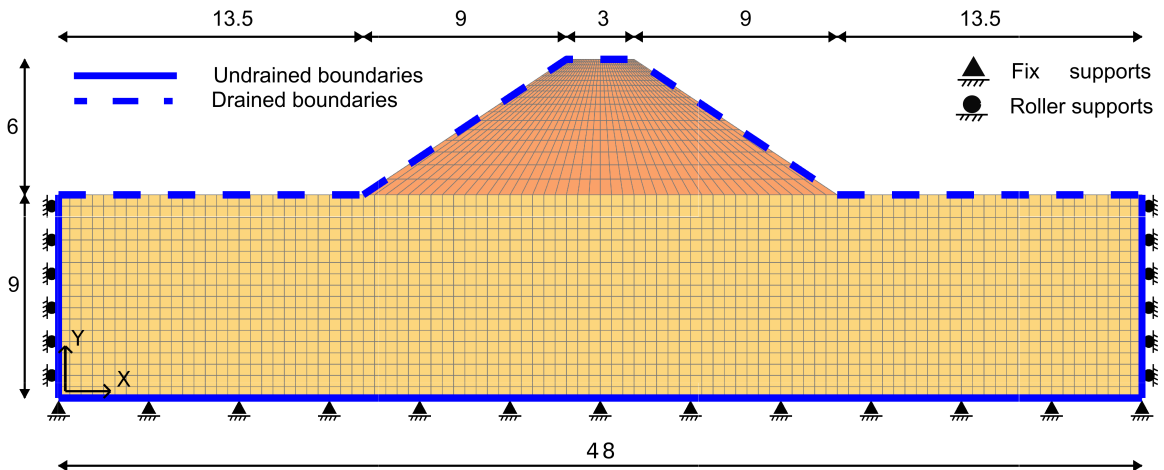


Figure 7: FEM mesh of the numerical model (Dimensions in m)

### 3.2. Constitutive model and parameter calibration

In this study, the behavior of liquefiable sand was modeled with the PM4Sand constitutive law which was developed by Boulanger and Ziotopoulou (2015). This model describes the plasticity of sand controlled by the stress ratio related to the critical state and the bounding surface (Dafalias and Manzari, 2004). The PM4Sand model has the capability of predicting the behavior of soil under cyclic loading for various relative densities. PM4Sand model requires 27 input parameters: 6 primary parameters and 21 secondary parameters (Boulanger and Ziotopoulou, 2015). The primary parameters include the relative density  $I_D$ , small-strain shear modulus coefficient  $G_o$ , contraction rate parameter  $h_{po}$ , the atmospheric pressure  $p_A$  and two 'flag' parameters (FirstCall and PostShake). There are variety of methods to estimate the small-strain shear modulus either by field tests (through empirical correlations with SPT or CPT tests) or from laboratory element tests (for example bender element test). In this study, the small-strain shear modulus coefficient  $G_o$  was directly estimated through the equations proposed by Azeiteiro *et al.* (2017) and Kassas *et al.* (2021b) for Hostun HN31 sand. The contraction rate parameter  $h_{po}$  can be calibrated with the experimental results in terms of the cyclic resistance curve ( $CRR - N$ ) of the sand. While the other secondary parameters can be either left with their default values or calibrated against the laboratory tests data (Boulanger and Ziotopoulou, 2015). In this study, the variable  $h_o$  that adjusts the ratio of plastic modulus to elastic modulus was taken as the minimum value 0.3, while the other secondary input parameters were left to their default values.

In the centrifuge model, although the same sand was used for the embankment and the liquefiable ground, according to the literature (Mulilis *et al.*, 1977; Tatsuoka *et al.*, 1986; Benahmed, 2001; Sze and Yang, 2014), the soil preparation method affects the liquefaction resistance. Therefore, when calibrating the PM4Sand model, it is essential to consider the effects of the preparation method *i.e.* the under-compaction method used for the liquefiable ground layer.

For the model parameters of PM4Sand which are not dependent on the sand preparation method *i.e.*  $G_o$ ,  $\phi$ ,  $Q$ ,  $R$ , the values proposed by Kassas *et al.* (2021b) were adopted (see Table 3). On the other hand, the contraction rate parameter  $h_{po}$ , which plays an important role in stimulating the liquefaction resistance of sand under cyclic loading, has to be calibrated carefully by taking into account the effect of the sand preparation method.

Table 3: Parameters used in the numerical model

Parameter		Value
Relative density	[%] $I_D$	50
Void Ratio	[-] $e = e_{\max} - I_D(e_{\max} - e_{\min})$	0.83
Shear modulus coefficient <sup>†</sup>	[-] $G_o = 293 \times \frac{(2.97-e)^2}{(1+e)}$	712
Critical state friction angle <sup>†</sup>	[°] $\phi$	33.8
Atmospheric pressure	[kPa] $p_A$	101.3
Lateral earth pressure <sup>†</sup>	[-] $K_0 = 1 - \sin \phi$	0.44
Poisson's ratio <sup>†</sup>	[-] $\nu = \frac{K_0}{1+K_0}$	0.3
Bolton's Constant <sup>†</sup>	[-] $Q$	8.4
Bolton's Constant <sup>†</sup>	[-] $R$	0.78
Permeability <sup>†</sup>	[m/s] $k = 2.92 \times 10^{-3} \times \frac{e^3}{(1+e)}$	$9.68 \times 10^{-4}$
Contraction rate parameter	[-] $h_{po}$	0.07
Secondary input parameter	[-] $h_o$	0.3

Note: The parameters marked with <sup>†</sup> were proposed by Kassas *et al.* (2021b) for Hostun HN31 sand prepared by dry air pluviation method.

The calibration of  $h_{po}$  was carried out against the experimental data of  $CRR - N$  curve of Hostun HN31 sand prepared by moist tamping method. For the  $CRR - N$  curve, since the direct data of undrained cyclic simple shear test of Hostun HN31 sand with humid under-compaction method was rare, thus the experimental data has to be obtained indirectly from other type of cyclic test *e.g.* triaxial cyclic test. In this study, the isotropically consolidated undrained cyclic triaxial tests on Hostun HN31 sand of Gobbi (2020) and Gobbi *et al.* (2022a,b) were converted to undrained simple shear  $CRR - N$  form by Eq. (1) proposed by Idriss and Boulanger (2008).

$$CRR = \frac{1 + 2K_0}{3} CRR_{TX} \quad (1)$$

where  $CRR$  is the cyclic resistance ratio in simple shear form;  $CRR_{TX}$  is the cyclic resistance ratio of cyclic triaxial test;  $K_0$  is the lateral pressure coefficient for simple shear test.

An empirical equation Eq. (2) was used to fit the converted undrained simple shear  $CRR - N$  data. Eq. (2) is based on the equation originally proposed by Kassas *et al.* (2021b), with modifications on the parameters. The contraction rate parameter,  $h_{po}$ , was then calibrated by conducting a series of numerical simple shear tests and matching the results with the  $CRR - N$  curve obtained from Eq. (2).

$$CRR = (-1.119 e + 1.14) N^{(0.24e-0.44)} \quad (2)$$

In this study, the simple shear test was carried out on a single element (SSPquadUP) under the initial vertical stress  $\sigma_v = 100$  kPa. The optimized value of  $h_{po}$  was found to be 0.07 and the calibration results are shown in Fig. 8. It is

shown that the calibration fits well with the curve globally. In case of higher  $CRR$  ratio ( $N$  ranges from 1 to 30) where the liquefaction is triggered after a few cycles, the fitting remains satisfactory. The main parameters of PM4Sand model used in this study are summarized in Table 3.

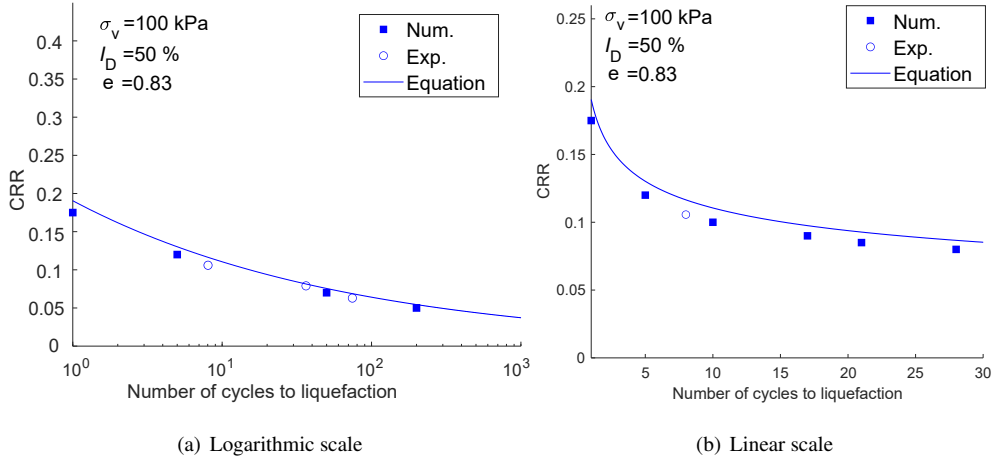


Figure 8: Calibration of PM4Sand constitutive model: Cyclic stress ratio vs. the number of cycles for liquefaction triggering

For the embankment soil, the Drucker-Prager model was adopted. As it was mentioned in section 2.4.3, the centrifuge model was saturated at 1g with viscous fluid. Due to the capillary effect, when the soil ground was fully saturated at 1g condition, the 100 mm height embankment was also partially saturated with viscous fluid, of which the water content is around 25%. According to Caicedo and Thorel (2014), when spin-up the centrifuge, due to the macro-gravity, the water content in the embankment can drop to around 2.0~3.5%, which was also confirmed by measuring the water contents of the samples taken from the embankment after the test. As a result of the unsaturated embankment and the viscous fluid, the cohesion and strength of the embankment soil increased. Therefore, in this study the peak friction angle  $38^\circ$ , the bulk modulus 173 kPa and the shear modulus 76 kPa were assumed as the parameters of the Drucker-Prager model for the unsaturated embankment soil according to Chen and Saleeb (1994). The cohesion of soil was set at 65 kPa in order to fit the settlement of the embankment as presented in Fig. 18 (see Section 5.4).

### 3.3. Procedure of numerical simulation

The numerical simulation was conducted on the FEM platform OpenSees – Version 3.2.2 64-Bit (OpenSees, 2020) in three steps. Firstly, the consolidation of the model was performed. At this stage, all elements' material properties were switched to elastic. Then, the material properties were switched from elastic to plastic and the "Update FirstCall" is activated and a "plastic gravity analysis" step was performed to initialize the internal variables and to reach the initial stress state of the model (see Section 2.6). After the consolidation, the whole model was subjected to dynamic shaking by "UniformExcitation" (Mazzoni et al., 2006). The numerical model was excited by the actual input signal applied in the dynamic centrifuge test, see Fig. 6. During the dynamic excitation, a Rayleigh damping ratio of 3.0% was

applied. The damping ratio was estimated through bender element test by the method proposed by Karl *et al.* (2008). The damping parameters were calculated with two modal frequencies 2.7 Hz and 6.7 Hz. These two frequencies were estimated by modal analysis with elastic material properties in Table 3.

In order to properly model the variation of the excess pore pressure, the hydraulic conductivity in the numerical model varied in two different stages: first, during the base shaking; and second, during the dissipation of excess pore pressure after shaking. During base shaking, the procedure proposed by Shahir *et al.* (2014) was adopted. The permeability was updated at each step according to Eq. (3), in which the permeability varied in function of the excess pore pressure ratio (Shahir *et al.*, 2014; Dinesh *et al.*, 2022; Basu *et al.*, 2022).

$$k = \begin{cases} k_b = k_i (1 + (\alpha - 1)r_u^{\beta_1}) & (\text{if } r_u < 0.95) \\ k_l = \alpha k_i & (\text{if } r_u \geq 0.95) \end{cases} \quad (3)$$

where  $k_i$  is the initial permeability of the soil;  $k_b$  is the permeability during the build up of pore pressure ( $r_u < 0.95$ );  $k_l$  is the permeability during liquefaction ( $r_u \geq 0.95$ ). The two constants  $\alpha$  and  $\beta_1$  were taken as 1.2 and 1, respectively, as they were proposed by Basu *et al.* (2022) for Hostun sand.

After the shaking, the "PostShake flag" in PM4Sand model was activated and the hydraulic conductivity was considered to decrease earlier before the excess pore pressure dissipation (Shahir *et al.*, 2012). It is recommended by Tobita (2020) that the permeability should decrease to a certain value lower than its initial value during the dissipation process. Therefore, Eq. (4) was used for the reduction of hydraulic conductivity, which starts at the middle of the last cycle of the input signal ( $t_2 = 18.1$  s) and ends at the last cycle ( $t_3 = 18.7$  s) as presented in Fig. 6(a). This equation is based on the one proposed by (Shahir *et al.*, 2012), but takes into account the reduction of permeability by a constant factor of  $\alpha_2$ .

$$k_d = \frac{k_i}{\alpha_2} (1 + (\alpha\alpha_2 - 1) \left( \frac{t - t_2}{t_3 - t_2} \right)^{\beta_2}) \quad (4)$$

where  $k_d$  is the permeability in the decreasing stage;  $t_2$  and  $t_3$  are the start and end time of decreasing stage, respectively; and the constants  $\alpha_2$  and  $\beta_2$  were taken as 40 and 1 in this study to have the best fit with the experimental results.

#### 4. Experimental results analysis

This section presents and discusses the main results of the dynamic centrifuge test. Firstly, the bender element test results before the base shaking are presented. Then, during the base shaking, the results are presented in terms of acceleration responses, the excess pore pressure ratio, liquefaction paths, *etc.* Finally, the model deformation and embankment failure pattern are discussed. All the experimental results hereafter are presented at the prototype scale unless otherwise mentioned.

#### 4.1. Bender elements results

The shear wave velocity  $V_s$  is calculated from the distance and the travel time of the shear wave between the transmitter and receiver. Concerning the determination of the travel time, different definitions of first arrival point are proposed in literature (Jovičić *et al.*, 1996; Lee and Santamarina, 2005; Murillo *et al.*, 2011; Kumar and Shinde, 2019). The travel time considered in this study is the time between the zero point of the input signal and the zero point after the first bump as proposed by Lee and Santamarina (2005) and adopted later by Kassas (2021). After the calculation of the shear wave velocity ( $V_s$ ), the small-strain shear modulus ( $G_{\max}$ ) was calculated using Eq. (5).

$$G_{\max} = \rho_{\text{sat}} V_s^2 \quad (5)$$

where  $\rho_{\text{sat}}$  is the mass density involved in the wave propagation. The estimated small-strain shear modulus was then compared with the empirical equation (Eq. (6)) proposed by Azeiteiro *et al.* (2017).

$$G_{\max} = 29300 \frac{(2.97 - e)^2}{1 + e} \left( \frac{p'}{100} \right)^{0.49} \quad (6)$$

It is shown in Fig. 9 that the experimental results and the empirical equation of  $G_{\max}$  were comparable, although dispersion was observed, which could probably be due to the precision of bender element measurement in the centrifuge test.

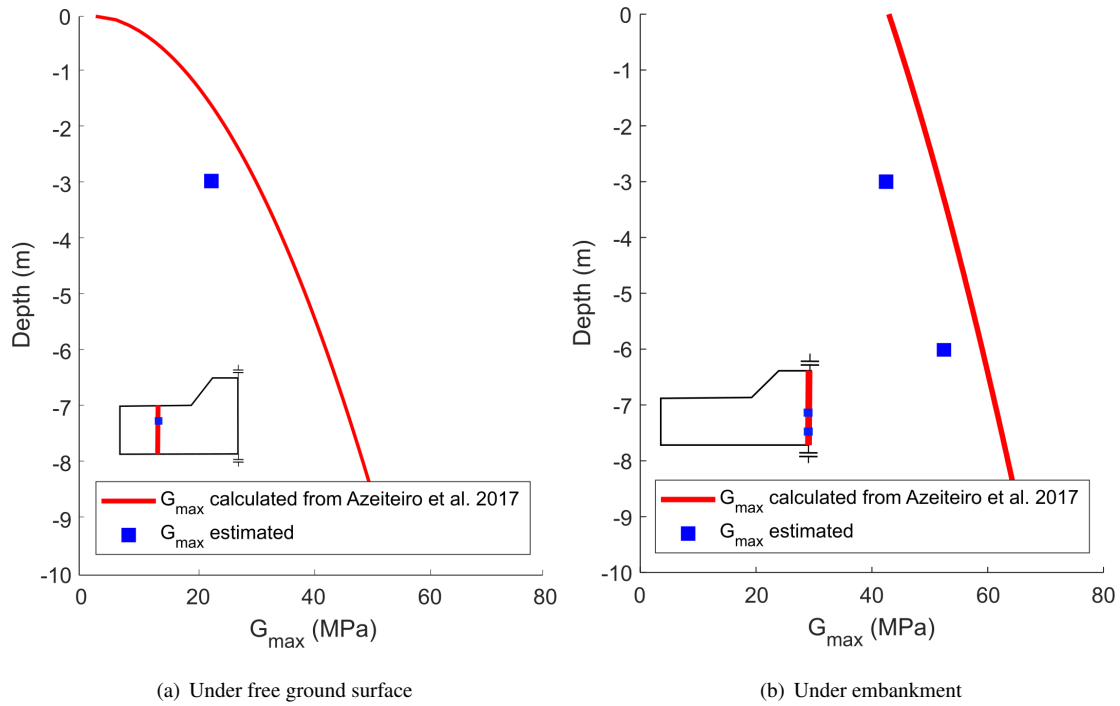


Figure 9: Comparison of the calculated small strain shear modulus with the empirical equation (Azeiteiro *et al.*, 2017)

#### 4.2. Acceleration response

The time-histories of acceleration response at different positions are compared to the base shaking input signal (Fig. 6), and the results are shown in Fig. 10. In this study, the noises and the unexpected frequency components in the signals (Fig. 6) were filtered by a band pass filter with the cut-off frequencies from 0.33 Hz to 6.67 Hz (at the prototype scale).

Different patterns of response were observed with the acceleration profiles. The first pattern was shown at bottom of the model (A2, A9, A12, A15, and A18) where the acceleration responses were very close to the input signal. This pattern proves the good transmission of the shear motion from the base of the container to the sand. An acceleration amplification effect is observed for A6, A7 and A8 which were embedded in the embankment, and the amplification increases from the bottom to the top. At A8, the amplification ratio with respect to the input signal is 2.12, with a phase lag of about 0.5 s. For the acceleration profiles beneath the toe of the embankment (A11, A14, A13, and A16), asymmetrical acceleration responses are observed, which indicates a horizontal movement of the embankment. These acceleration responses are in accordance with the work of [Adalier and Sharp \(2004\)](#). These positive spikes were caused due to the irregular geometry of the model above these positions. The acceleration profiles in Fig. 10 also reveal that liquefaction has occurred in the free ground rather than in the soil beneath the embankment. It is clear that the accelerations at A17 and A20 show a significant attenuation after two cycles, where the liquefaction occurred and the shear waves cannot be transmitted. This behavior is in accordance with the study of [Koga and Matsuo \(1990\)](#) for embankments resting on liquefiable sandy ground.

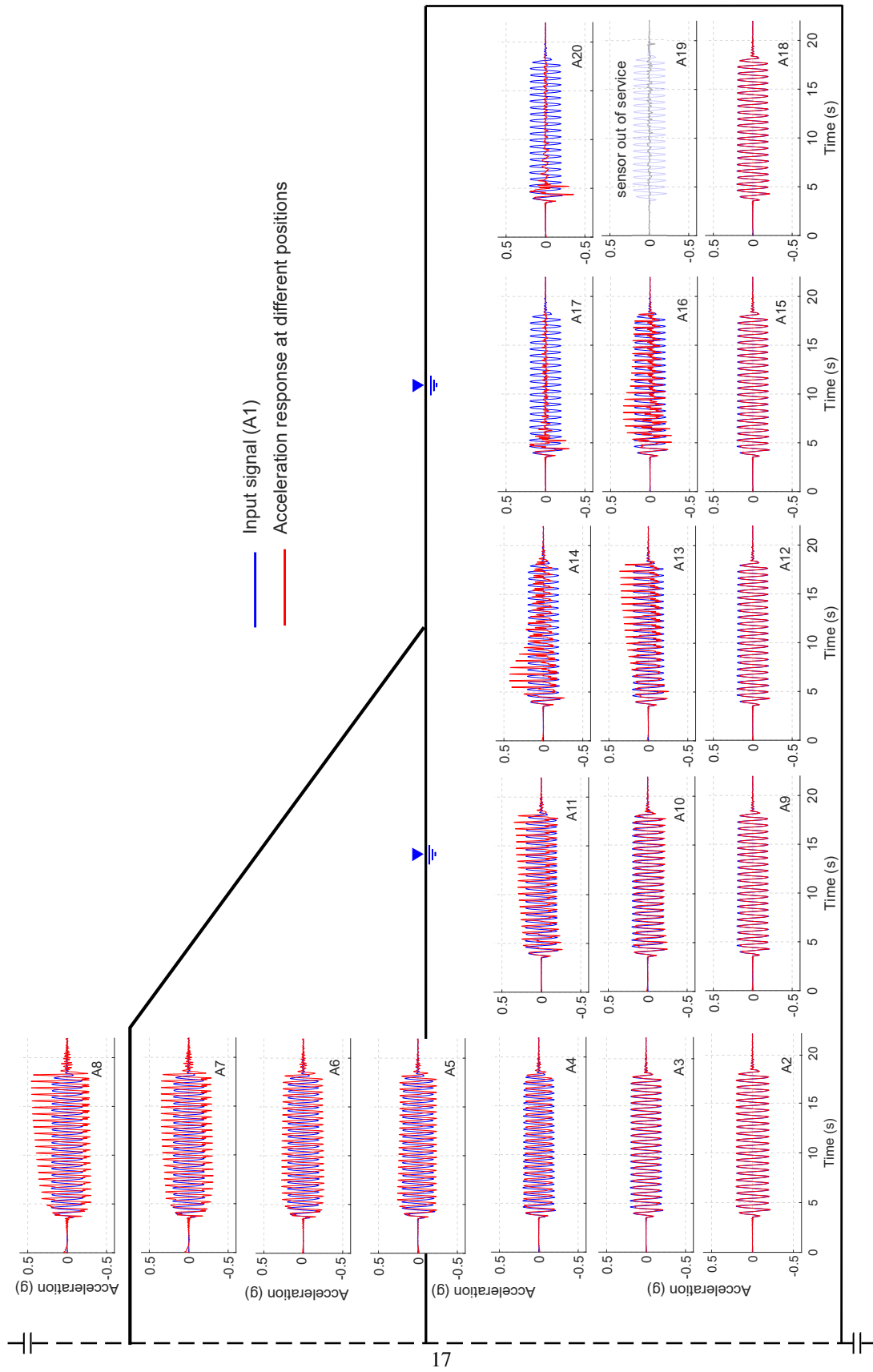


Figure 10: Acceleration responses at different positions in the model during dynamic excitation



#### 4.3. Excess pore pressure response

The variation of excess pore pressure ratio  $r_u$  (ratio between excess pore pressure and initial vertical effective stress) at various locations in the model is shown in Fig. 11. Below the embankment (P1 to P8), the evolution of the pore pressure ratio follows the same tendency. In terms of  $r_u$ , the excess pore pressure reaches approximately 50% of the initial vertical effective stress, which indicates that the soil beneath the embankment was not liquefied. While for P10 and P11 under the free ground, the  $r_u$  increased rapidly after approximately two cycles and reached 1, which indicates the occurrence of liquefaction. The responses of excess pore pressure at P10 and P11 are in accordance with the acceleration responses presented in section 4.2 and confirm again the preference of liquefaction at the free ground (Koga and Matsuo, 1990).



and 4.3. Due to the presence of the embankment, which results in higher effective vertical stress, liquefaction did not occur under the embankment. In contrary, at a distance from the embankment where the effective confining pressure was relatively low, liquefaction occurred.

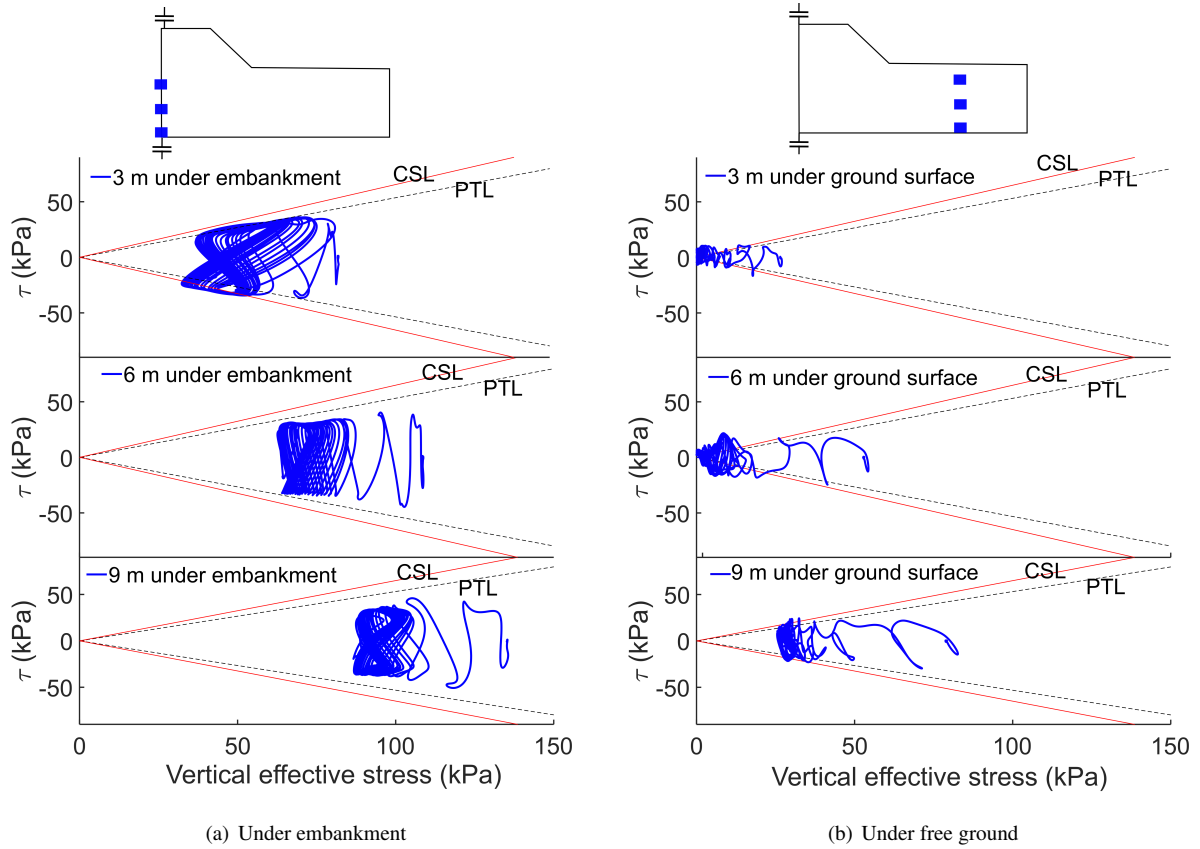


Figure 12: Stress paths at different positions (a) under embankment and (b) under the free ground surface. CSL and PT are Critical state Line and Phase Transformation Line for Hostun HN31 sand (Benahmed, 2001), respectively.

#### 4.5. Model deformation and embankment failure pattern

Fig. 13 (a) shows the profiles of the maximum dynamic lateral displacement calculated by the double integration (Li *et al.*, 2013) of the recorded accelerations at different vertical arrays: center of the model (black line), under the toe of the embankment (red line) and under free ground surface (blue line). As it is shown in Fig. 13 (a), in the ground soil layer, the lateral displacement increased significantly around 6 meters under the ground surface. On the other hand, in the embankment, the slope of the maximum displacement profile above the ground surface decreased, which indicates a small relative displacement between the soil layers in the embankment. The maximum shear strains at different arrays in Fig. 13 (b) confirm a peak value at the depth around 6 m under the free ground; while for the embankment, the maximum shear strain decreased. As it was explained in section 4.4, limited and full liquefaction were observed under the embankment and under the free ground, respectively. The liquefaction of the soil caused a

306 decrease in the shear resistance, which results in a “soft” and “slippery” ground, on which the embankment moved  
 307 approximately as a rigid block and exhibited a lateral sliding behavior.

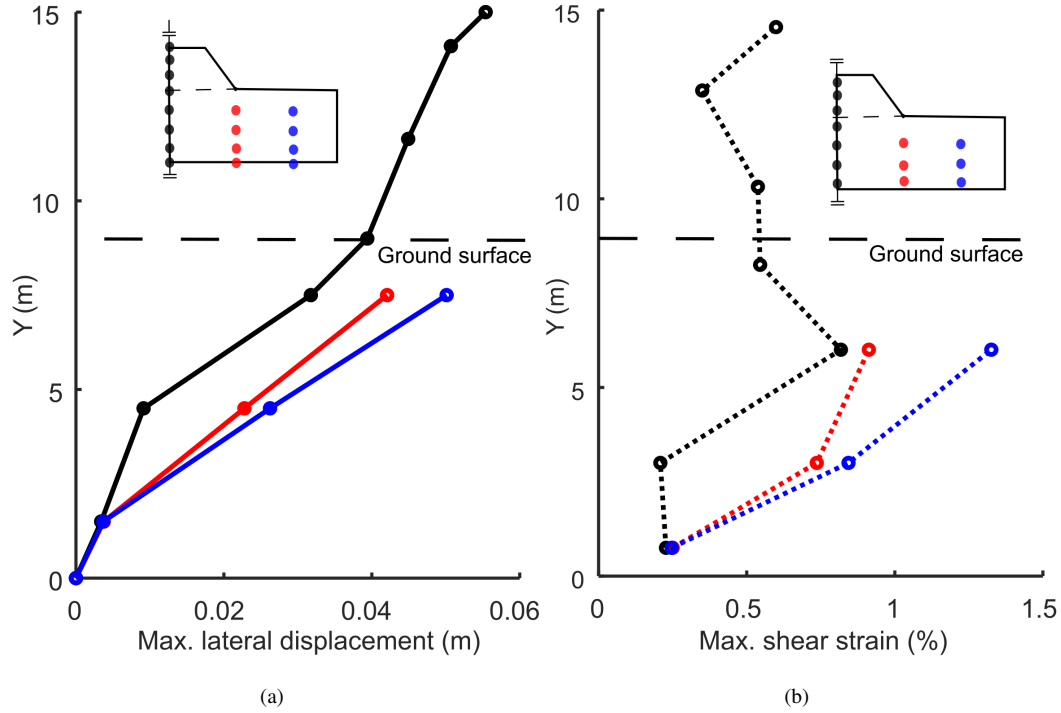


Figure 13: Displacement and shear strain analyses: (a) Maximum dynamic lateral displacement and (b) maximum dynamic shear strain at different positions in the model

308 Fig. 14 shows the deformation of the embankment before and after the base shaking and the settlements recorded  
 309 by D1, D2 and D3 (Due to the symmetry of the model, the results of D4 and D5 are close to those of D2 and D3).  
 310 A great crest settlement was observed, which is noted by the dashed lines in Figs. 14 (a) and (b). The recorded  
 311 crest settlement was recorded by the laser sensors D1 (Fig. 14 (c)). The crest settled around 0.7 m which was nearly  
 312 12.0% of the embankment height. This settlement was accompanied by a 0.2 m settlement of the middle slope of the  
 313 embankment shown in Fig. 14 (d). In addition, a heaving of 0.04 m was observed at the free ground surface near the  
 314 toes, see Fig. 14 (e). The heaving observed near the toes indicates a possible lateral spreading of the toes embankment  
 315 (Fig. 14 (f)). The deformation pattern agrees well with the results reported by Doboku (1986), Oka *et al.* (2012),  
 316 Adalier and Sharp (2004), Shahbodagh *et al.* (2020) and Li *et al.* (2021).

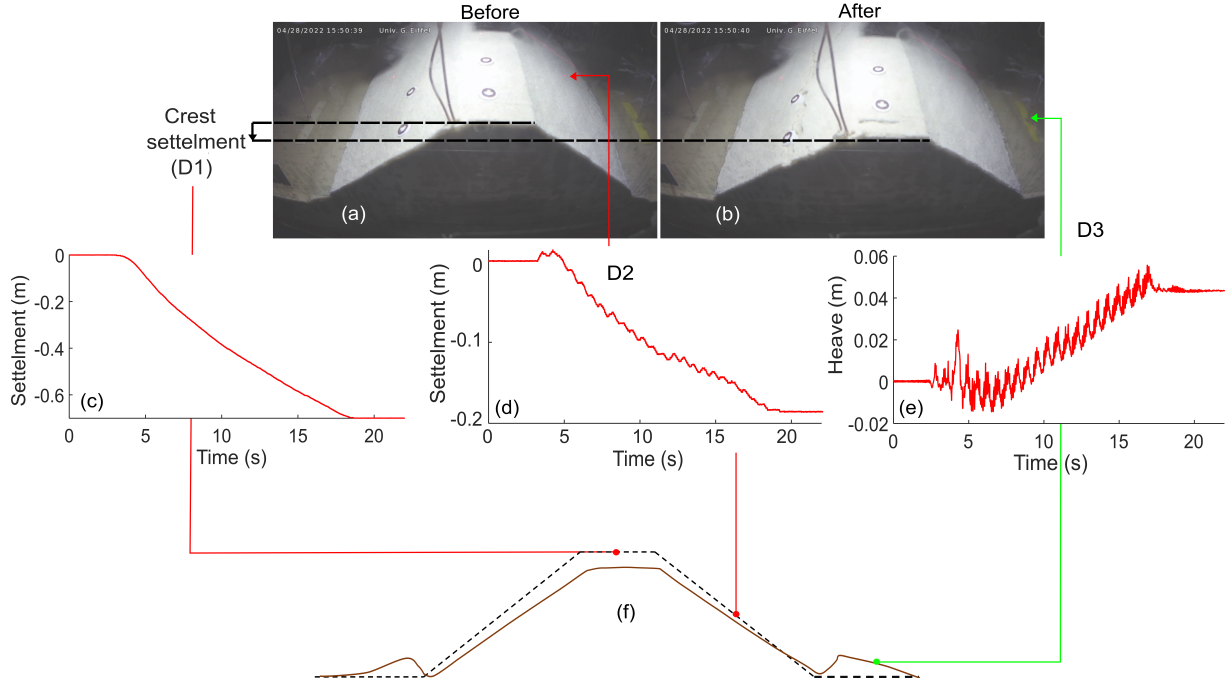


Figure 14: Deformation and settlement analyses: photos (a) before and (b) after the base shaking; (c) D1, Settlement of embankment crest; (d) D2, settlement of the middle slope of the embankment; (e) settlement at the free ground surface measured by potentiometer D3 and (f) embankment deformation pattern

## 5. Performance verification of the numerical model – comparison of numerical and experimental results

The performance of the numerical model was verified by comparing the numerical results with the experimental results. The comparisons were conducted for the time-histories of acceleration, excess pore pressures and the deformation of the embankment, which are presented hereafter.

### 5.1. Acceleration response

Based on Anderson's Goodness of Fit (GoF) criteria (Anderson, 2004), the acceleration times histories computed with numerical model were compared to the experimental data. Quantitative scores were estimated to classify the agreement into poor fit (score lower than 4), fair fit (score between 4 and 6), good fit (score between 6 to 8) and excellent fit (score higher than 8) (Santisi d'Avila and Semblat, 2014). The score  $S$  related to the parameter  $p$  was estimated between numerical ( $p_n$ ) and experimental results ( $p_e$ ) using Eq. (7)

$$S\{p_n, p_e\} = 10 \exp\left(-\left(\frac{p_n - p_e}{\min(p_n, p_e)}\right)^2\right) \quad (7)$$

The items used for comparison of the time-histories acceleration at different positions are the peak acceleration (Spga), peak velocity (Spgv), peak displacement (Spgd), arias intensity (SIa), energy integral (SIv), acceleration

spectral (Ssa, 5 % damping) and the Fourier spectra (Sfs). The comparison of numerical and experimental results was carried out for signals filtered with a band pass filter (0.33 Hz~6.67 Hz). The total score for a specific position is considered as the mean value of all scores calculated at this position.

Fig. 15 and Table 4 show the comparison of the acceleration responses between experimental and numerical results at different positions: at embankment crest (A8), under the embankment (A3), near embankment toe (A14) and under the free ground surface (A17). Overall, the computed acceleration time histories are in good agreement with the measured acceleration in the centrifuge test.

For A3 under the embankment, a symmetrical acceleration profile is observed in the centrifuge and in numerical model which is classified as an excellent fit. The numerical model accurately simulated the experimental results in the central part of the model beneath the embankment, where liquefaction did not occur. At the embankment crest, the acceleration (A8) computed with numerical model is in good accordance with the experimental results. Overall, the scores are good, despite of the fair score of the acceleration spectral (Ssa). This low score can be explain by the underestimation of the acceleration amplitude after the third cycle which is observed in time histories acceleration. The observed difference at A8 could be attributed to the constitutive law utilized for the embankment. As mentioned before, the embankment was in an actual unsaturated state, and the Drucker-Prager model employed can only approximately simulate the behavior of the unsaturated embankment as a simplified “ $c - \phi$ ” soil. Thus, the transmission of the shear wave in the unsaturated embankment cannot be effectively captured by the numerical model. In addition, the response under the toe of the embankment (A14) which is characterized by an asymmetrical acceleration is also captured in a good way by the numerical model. The numerical model successfully captured the asymmetrical response, but it underestimated the acceleration amplitude in the positive part. This discrepancy may be attributed to the same cause that affects the prediction of the acceleration at the embankment crest (A8). The difference in amplitude after the first three cycles could be attributed to the limitations of the Drucker-Prager model when simulating the unsaturated soil. Under the free ground surface, the comparison between numerical and experimental results at position A17 shows some differences. These differences were classified as an overestimation of the acceleration amplitude after two cycles which was also reflected by the scores of the peak acceleration (Spga) and arias intensity (SIa). These differences of the amplitude after two cycles, when the initiation of the liquefaction occurred, could be attributed to the boundary effect of the numerical model.

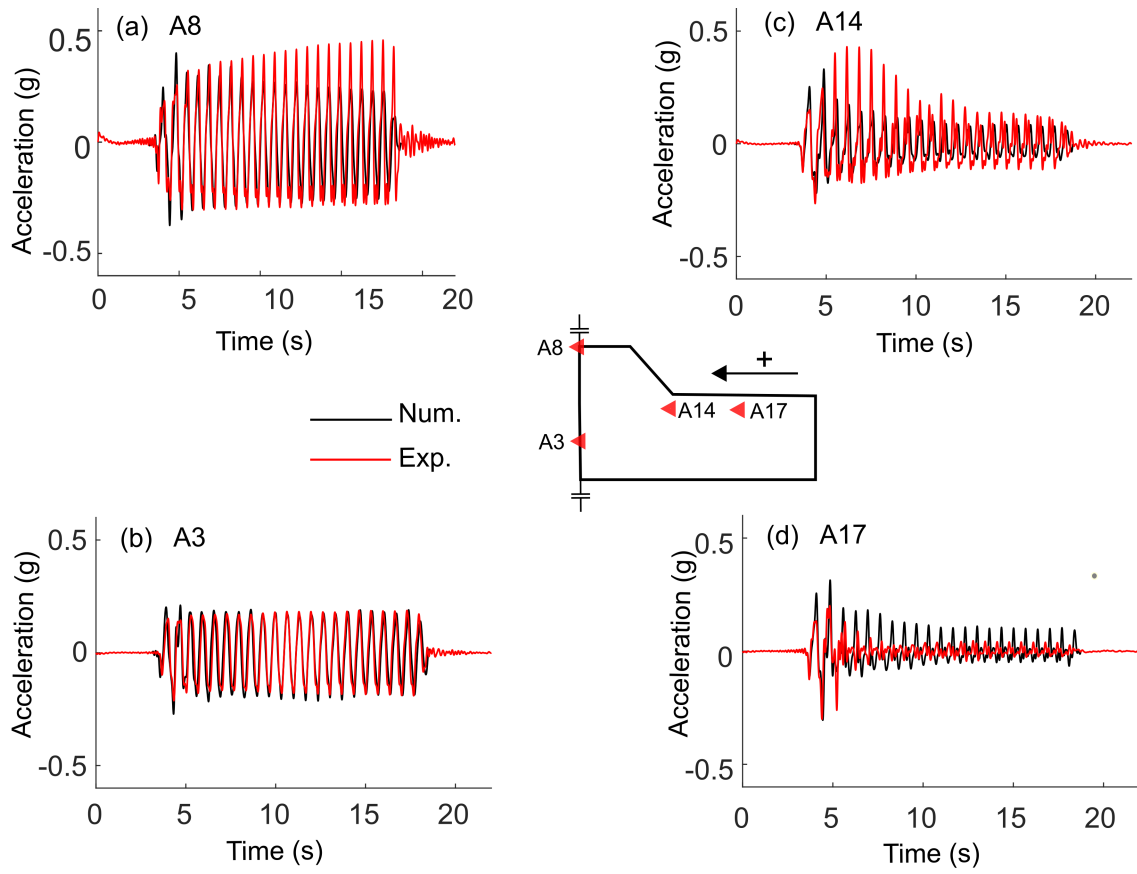


Figure 15: Comparison of numerical results with experimental results in centrifuge test in terms of acceleration response (a) at the embankment crest (b) under the embankment (c) near the embankment toe and (d) under the free ground surface

Table 4: Scores of Anderson's Goodness of Fit classification at different positions (A17, A14, A8 and A3). Comparison of different parameters SIa (Arias intensity), SIv (Energy integral), Spga (Peak acceleration), Spgv (Peak velocity), Spgd (Peak displacement), Ssa (Acceleration spectra (5% damping)) and Sfs (Fourier spectra). (A) Excellent (B) Good (C) Fair and (D) Poor.

Position	SIa	SIv	Spga	Spgv	Spgd	Ssa	Sfs	Total score
A17	D	A	B	A	B	A	D	<b>B</b>
A14	D	A	A	A	B	A	D	<b>B</b>
A8	A	A	A	B	A	D	D	<b>B</b>
A3	A	A	A	A	C	B	D	<b>A</b>

## 5.2. Excess pore pressure ratio

The numerical and experimental results of excess pore pressure ratio are compared in Fig. 16 for two positions under the embankment (Figs. 16 (a) and (b)) and two other positions under the free ground surface (Figs. 16 (c) and (d)). The numerical model captured the variation of excess pore pressure at the positions P5 and P8 under

the embankment. In the case of pore pressure P5 under the embankment, the excess pore pressure ratio was well simulated for the first six cycles, but for the subsequent cycles, the model underestimated the excess pore pressure ratio. This may be attributed to the limitations of the current numerical model in accurately simulating the changes in pore pressure in the zone (near P5) where the soil transitioned from a fully saturated to a partially saturated state. At the positions P10 and P11, the numerical model captured well the build-up and also the dissipation of excess pore pressure under the free ground surface.

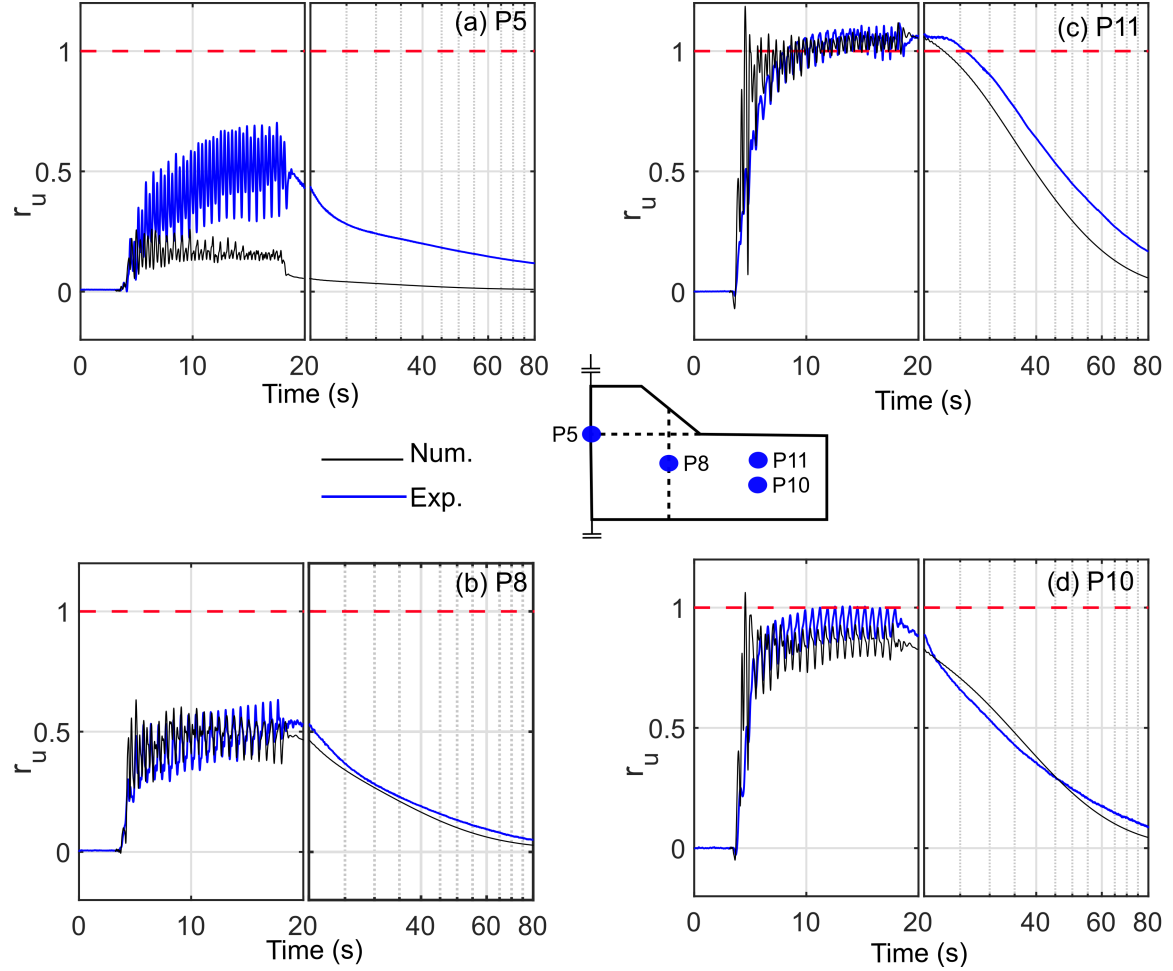


Figure 16: Comparison of numerical and experimental results in terms of excess pore pressure ratio under the embankment (a) P5 and (b) P8; under free ground surface (c) P11 and (d) P10

### 5.3. Stress path of liquefaction

The stress paths calculated from the experimental data were compared to those extracted directly from the elements of the numerical model in Fig. 17. The numerical model captured a rapid decrease in the effective stress under the free ground surface as well as the mobilization and stabilization of the effective stress under the embankment. In terms of the number of cycles before liquefaction occurs, the numerical results indicate that liquefaction initiates



after one cycle. This is earlier than what was observed in the centrifuge test, where liquefaction occurred after two cycles. It should be noticed that the liquefaction stress paths in the experiment were calculated from the 1D horizontal accelerations and the excess pore pressure nearby, which were not as precise as the stress paths obtained directly from the individual elements of the FEM model.

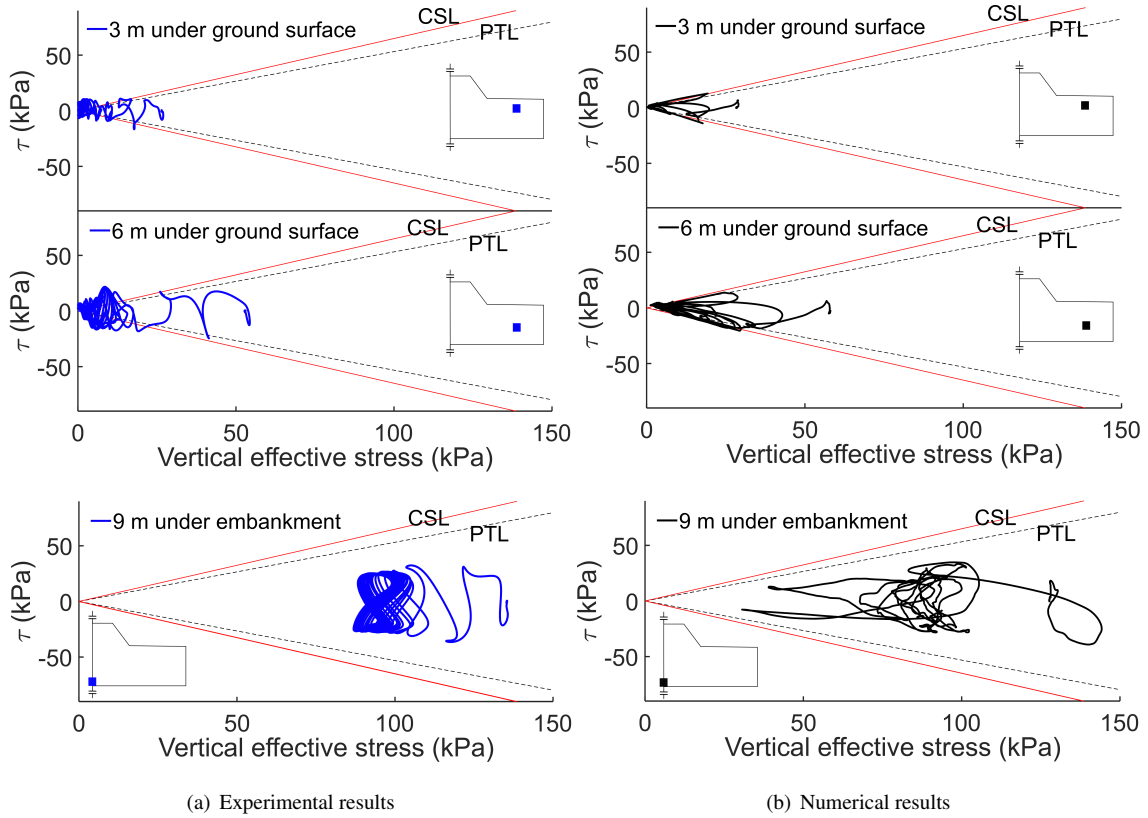


Figure 17: Stress paths of liquefaction under the free ground surface and under the embankment (a) obtained from the centrifuge test and (b) computed by the numerical model

#### 5.4. Settlement and deformation

Fig. 18 compares the numerical and experimental results for the settlements of the embankment crest and free ground surface, including a parametric study that investigates the influence of the cohesion of the embankment soil on embankment settlement. In this study, the optimum value was selected for a good fit with experimental results. According to the parametric study shown in Fig. 18, it is found that the cohesion does not only influence the deformation of the embankment itself, but also the settlement of the free ground surface. The numerical model reflects the settlement and deformation trends that observed in the centrifuge test. Quantitatively, the settlement of the embankment crest measured in the centrifuge test is about 0.7 m, which is also captured by numerical model with 65 kPa of the cohesion. However, the heaving of the free ground surface from the numerical model using the selected cohesion (about 0.25 m) was larger than the experimental result (about 0.04 m). The significant difference in ground surface

heaving may be due to the influence of the rigid numerical boundary conditions. Additionally, the difference may be attributed to the presence of the self-weight of the potentiometer which can increase the settlement and at the same time limit the heaving during the centrifuge test. For the model deformation pattern, the response of the numerical is presented in Fig. 19 at the end of shaking ( $t=18.26$  s). As explained before, there was no important liquefaction of soil beneath the embankment as it is shown in the contour plot of the excess pore pressure distribution. For the soil under the free ground surface, the excess pore pressure increased largely and reached the maximum value, which indicates the liquefied zones (in yellow). The liquefied zones, which extend from the toes of the embankment to the free ground surface, result in lateral displacement of the soil beneath the embankment and significant embankment settlement. In addition, a lateral displacement of the toes of embankments was observed followed by the heaving of the free ground surface.

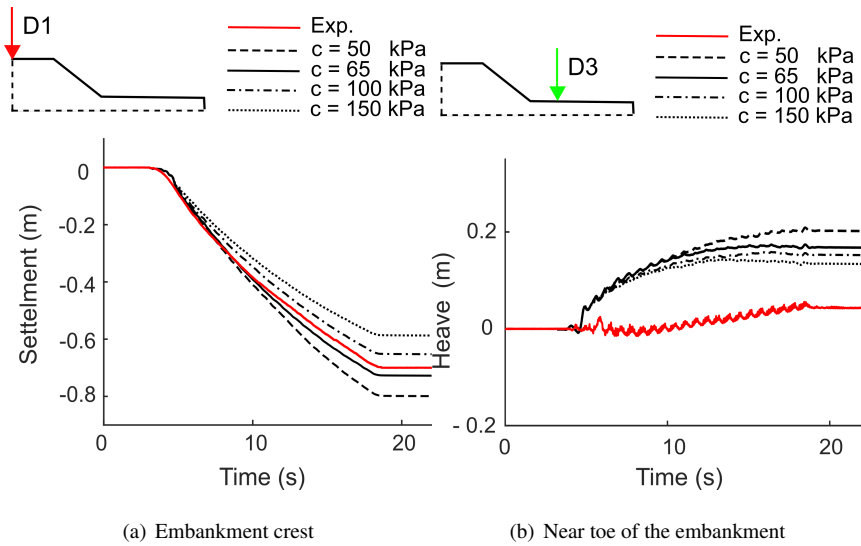


Figure 18: Settlements from numerical simulation and centrifuge test at the: (a) embankment crest and (b) free ground surface

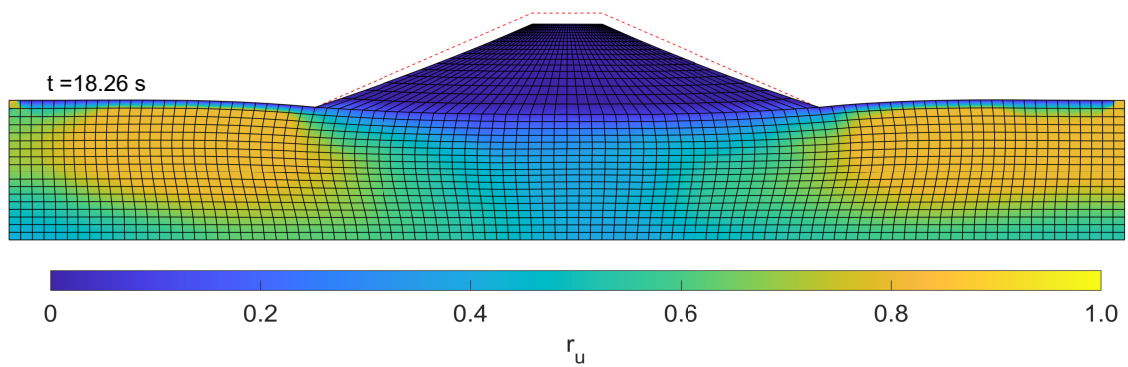


Figure 19: Deformation of the model and the distribution of excess pore pressure at the end of shaking ( $t=18.26$  s)

## 6. Study of the influence of the boundary conditions on the responses of the model

The numerical model presented in section 5 was built exactly based on the dimensions and the boundary conditions of the centrifuge model. The model shows good performance in terms of acceleration, excess pore pressure, settlement and deformation. However, due to the limited dimension of the model, the results could be possibly influenced by the boundaries. In order to clarify and quantify these influences and their impacts on the model responses, two new models were built in this section (see Fig. 20): the first model with the free field conditions and the second model with extended lateral boundaries.

The first model is similar to the original model presented in section 3, but the boundaries on the lateral side were changed from rigid to flexible conditions. The flexible free-field conditions (or periodic boundary conditions (Basu *et al.*, 2022)) were realized by imposing the same displacement on the nodes at the same depth by command “EqualDOF” in OpenSees.

For the second model, the original model was extended by 150 m for each side of the ground soil as shown in Fig. 20. According to the analyses of Kassas (2021) and Kassas *et al.* (2021a) on the boundary effect of a rigid container, when the ratio of the boundary distance to the soil depth is larger than 8, the boundary effect of a rigid container is negligible. In this study, for the model with extended boundaries, the ratio between the distance of the embankment toe to the side and the ground soil depth is around 18.2. Therefore, it could be regarded that the boundaries do not affect the response of the embankment or the soil in its vicinity in the extended model. The new extended model keeps the same boundary conditions as the original model. The extended parts were modelled with the same type of element and material constitutive law. The same analysis procedure explained in section 3.3 was adopted.

In order to investigate the influence of the boundary condition on the response of the model, this section focuses on the comparison of experimental results with the three numerical models in terms of acceleration, excessive pore pressure, and settlements.

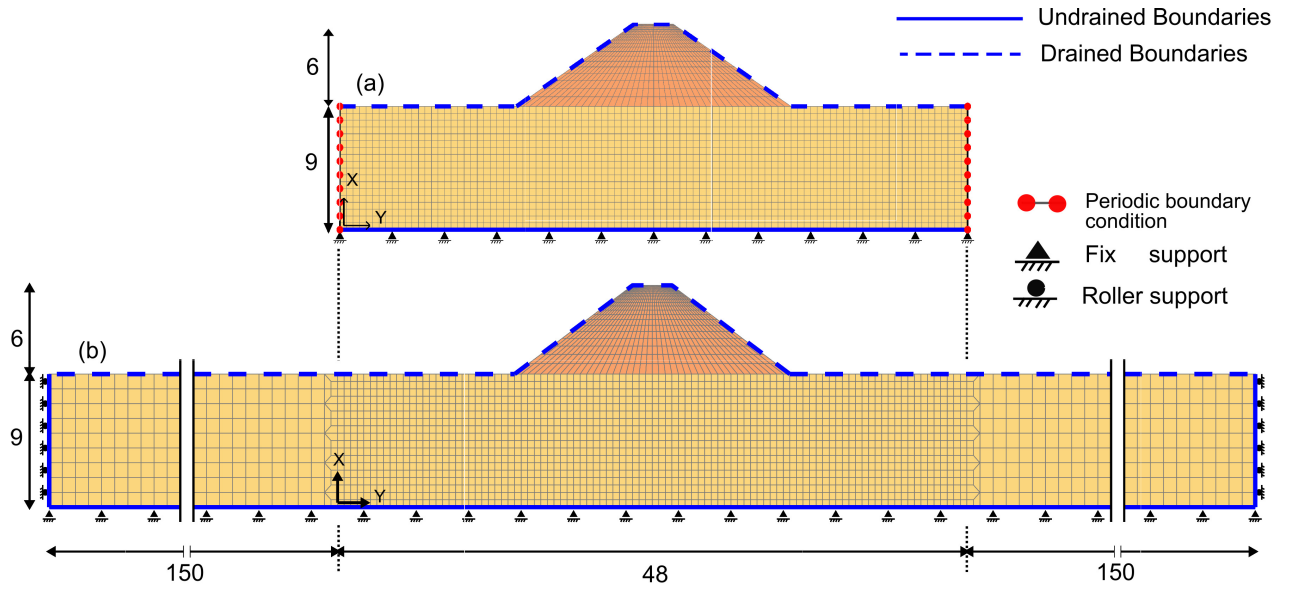
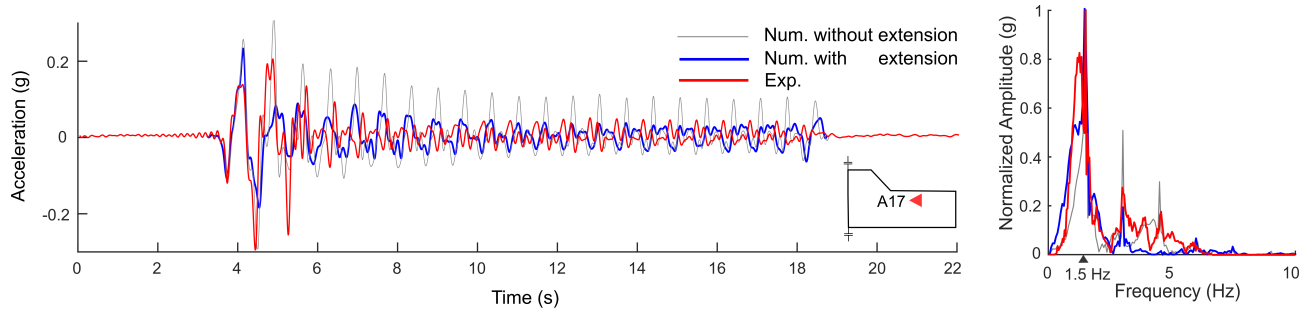
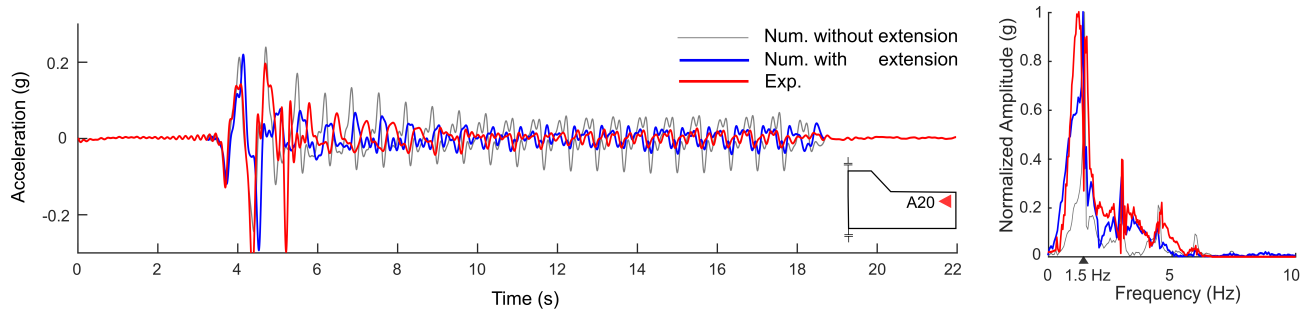


Figure 20: FEM mesh of the new models: (a) with free field conditions and (b) with extended boundaries of the ground soil (unit in prototype scale)

In terms of acceleration responses under the free ground surface (A17 and A20), Fig. 21 presents the comparison between the results obtained from the original model and the extended model; while Fig. 22 shows the comparison between the results obtained from the original model and the model with flexible free-field conditions. The numerical results from different models were also compared with the experimental results. The accelerations recorded during centrifuge test and those computed with numerical models show the same dominant frequency around 1.5 Hz in prototype scale. In terms of the time-history representation, the accelerations show similar trends for experimental and numerical models in which the amplitude decreases after two cycles. By quantifying the amplitude, the results obtained by the two new models (with extension and with free field condition) are closer to the experimental results and are better than the results from the original model. Overall, the original model can capture the main features of the experimental results, its responses are not significantly different from the two new models which have the more realistic boundaries. This indicates that (a) for the original numerical model, although certain boundary effects were observed, the numerical boundary conditions do not greatly affect the acceleration responses and (b) the rigid container used in the test did not affect significantly the behavior of the centrifuge model.



(a) Accelerations at A17



(b) Accelerations at A20

Figure 21: Comparison of experimental and numerical results (original model and model with extensions) in terms of amplitude and normalized frequency content of the acceleration at different positions: (a) A17 below the soil surface near embankment toe and (b) A20 near the container boundary

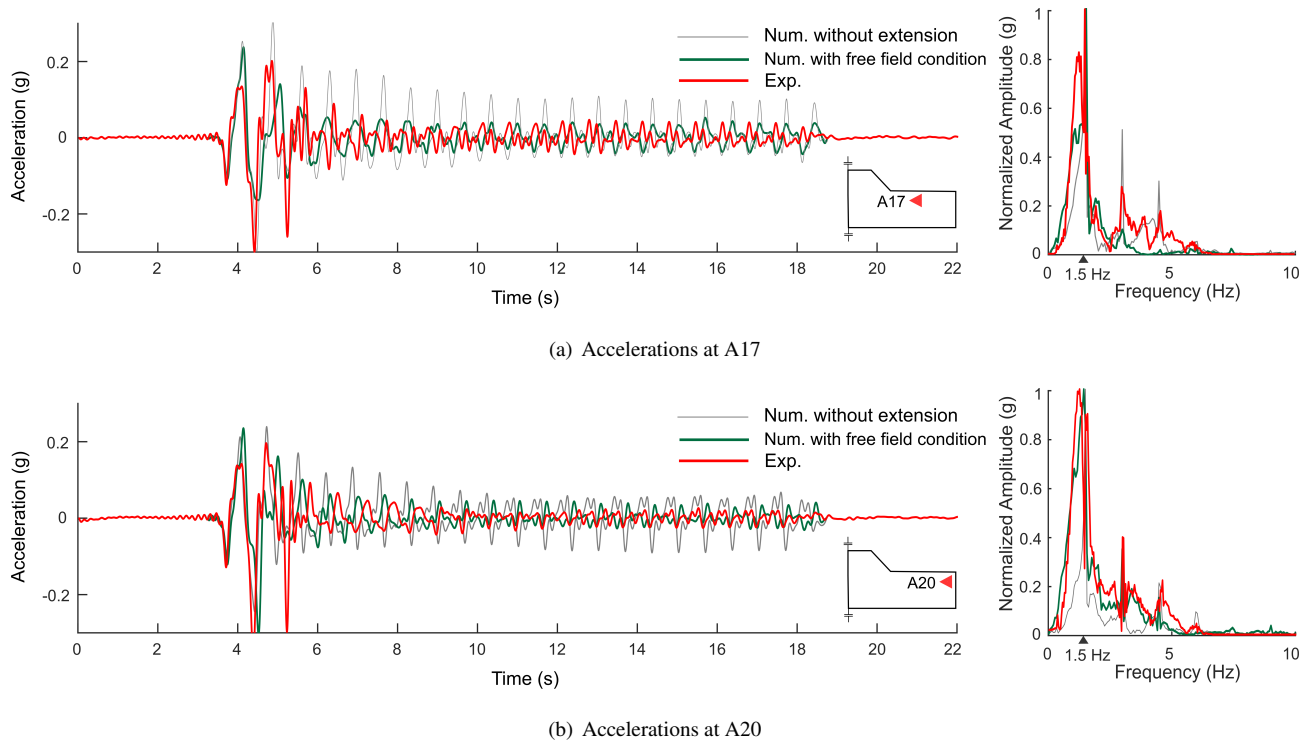
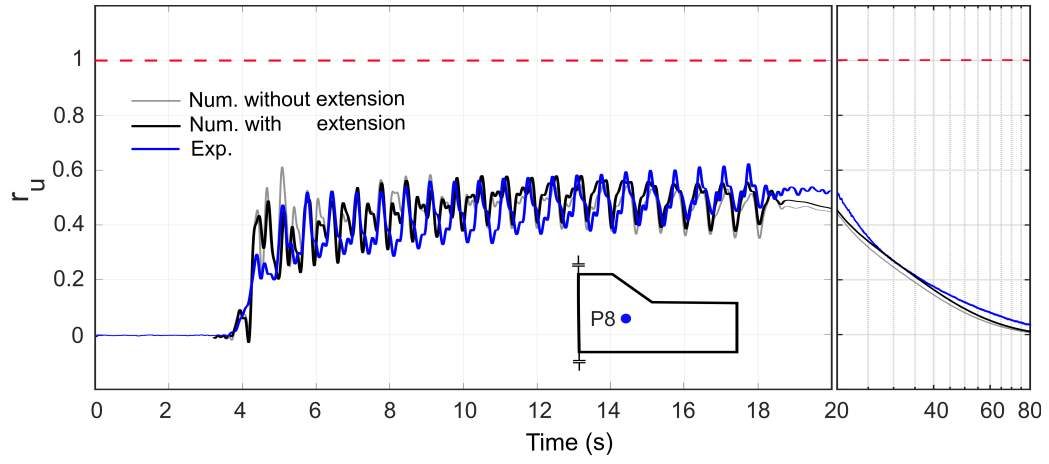


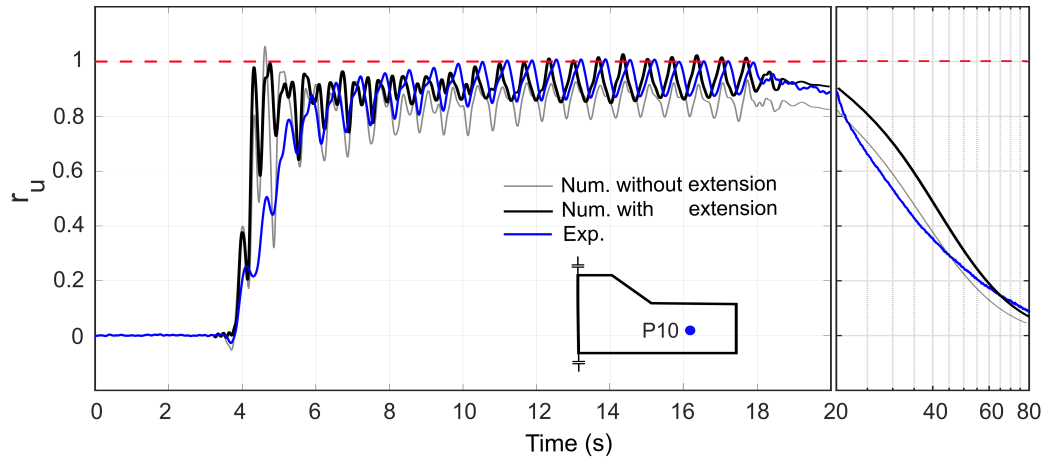
Figure 22: Comparison of experimental and numerical results (original model and model with free field condition) in terms of amplitude and normalized frequency content of the acceleration at different positions: (a) A17 below the soil surface near embankment toe and (b) A20 near the container boundary

The excess pore pressures obtained from the two new models were compared with experimental results in Fig. 23 and Fig. 24. Under the embankment (P8), the excess pore pressure ratios obtained by the extended model and model with free field conditions are similar to the original numerical model and the experimental results. It indicates the numerical boundary conditions or the original model and the rigid lateral sides of the container used in the centrifuge test did not affect significantly the pore pressure response under the embankment.

For the position near the boundary of the container (P10), the build-up and dissipation of excess pore pressure computed with the three numerical models are comparable to each other and are also comparable to the experimental results. Under the free ground surface, the pore pressure increased rapidly (with  $r_u \geq 0.9$ ) after 2 cycles. The liquefaction initiation was captured by the numerical models which is in accordance with the experimental results. This indicates that the numerical boundary conditions of the original numerical model and the rigid container used in centrifuge test did not have significant impacts the variation of pore pressure for the locations under the free ground surface.

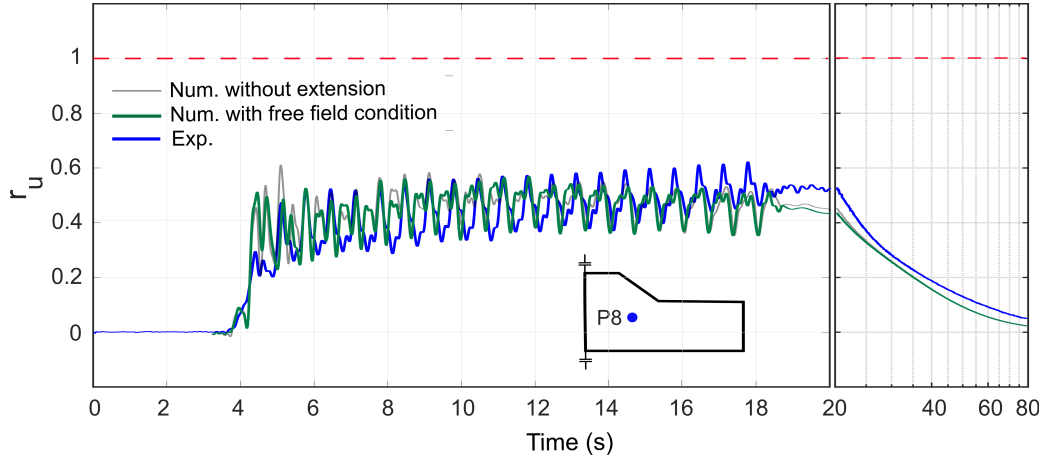


(a) Excess pore pressure at P8

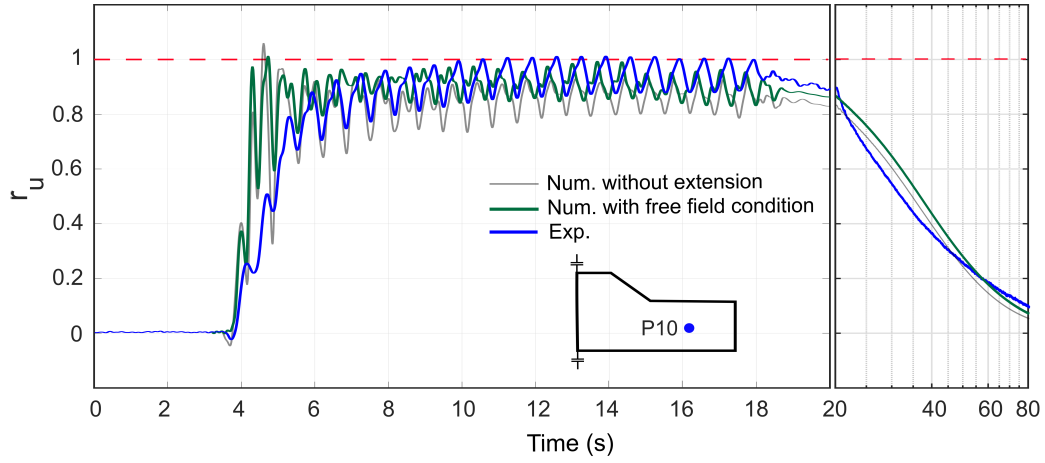


(b) Excess Pore pressure at P10

Figure 23: Comparison of experimental and numerical results (original model and model with extensions) in terms of excess pore pressures at different positions: (a) P8 under embankment and (b) P10 below the ground surface



(a) Excess pore pressure at P8



(b) Excess Pore pressure at P10

Figure 24: Comparison of experimental and numerical results (original model and model with free field condition) in terms of excess pore pressures at different positions: (a) P8 under the embankment and (b) P10 under the free ground surface

The embankment deformation and ground surface displacement recorded during the experimental test were also compared to the results of the three numerical models (with free field condition, with and without extension). The comparison is shown in Fig. 25. The deformation pattern was similar in all models: the embankment crest settled, accompanied by the heaving of the ground surface at a distance from the embankment toe (also observed in Fig. 26). At the embankment level, the settlement of the crest obtained by the model with free field condition (0.72 m) is similar to those of the model without extensions (0.70 m) (Fig. 25 (a)).

For the free ground surface near the toes of the embankment, the heaving simulated by the free field condition model (0.21 m) is close to the heaving in the original numerical model (0.23 m). For the model with extended boundaries, the crest settlement (0.82 m) is slightly larger than the others (experimental, original numerical model and free field condition model). The computed heave (0.14 m) is improved but still higher than the experimental results



(0.04 m).

Therefore, for the two models without extensions, the numerical boundary conditions affect slightly the crest settlement and the heaving of free ground surface as shown in Fig. 25 (b). However, for the numerical model with extensions, although the simulation of heaving on the free ground surface is improved, a slight overestimation of the crest settlement is observed.

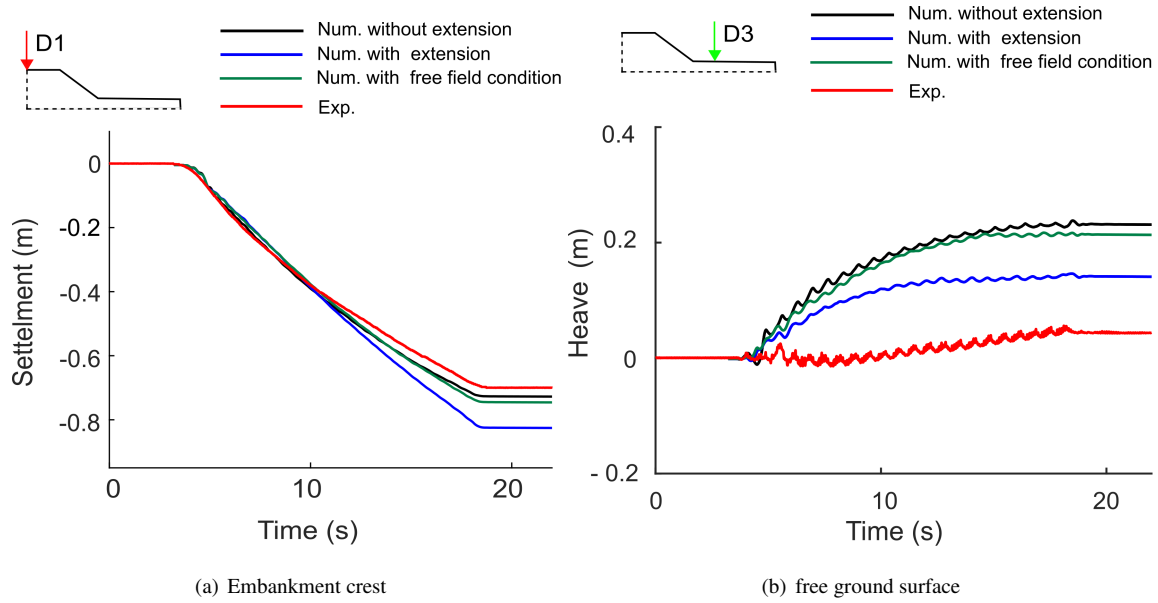


Figure 25: Vertical displacement at: (a) embankment crest and (b) free ground surface near the toe of embankment

Furthermore, the deformation and the distribution of the excess pore pressure ratio of the three numerical models were presented in Fig. 26 after the shaking ( $t=18.26$  s). A similar deformation pattern was observed in the three models. Under the embankment, the excess pore pressure distribution has the same pattern for the three models. Under the free ground surface, the pore pressure distribution was similar in the three models up to a distance of around 5 m away from the lateral sides (marked in red in Fig. 26 (a)). In this zone, the pore pressure ratio obtained by the numerical model was less than those of the other two models. This difference allows to define the zone affected by the numerical boundaries (Saade *et al.*, 2022). For the positions close to the lateral sides of the container, due to the influence of the boundaries, the liquefaction potential decreases.

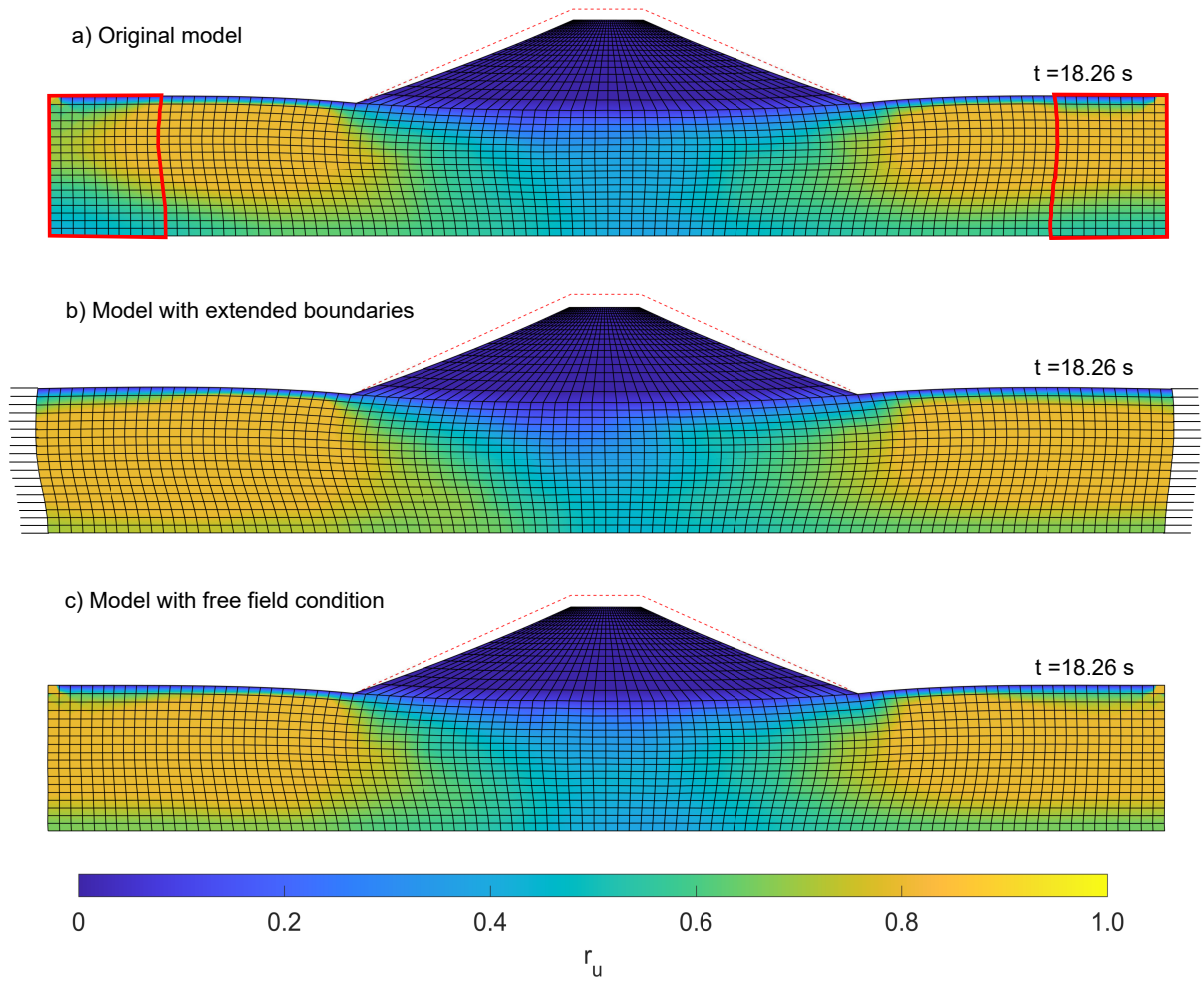


Figure 26: Deformation and the distribution of excess pore pressure at the end of shaking of the 3 numerical models: a) original model b) model with extended boundaries and c) model with free-field conditions

## 7. Conclusions

In this study, a dynamic centrifuge program was performed to have the direct observation and analysis of the behavior of a homogeneous embankment resting on liquefiable ground. Additionally, FEM numerical modeling was carried out using an advanced constitutive model – PM4Sand, and the performance of the numerical model was verified against the experimental results. With the verified numerical model, the boundary effects in the numerical simulation and dynamic centrifuge test were analysed and discussed. Based on the experimental and numerical results, the following conclusions can be drawn:

- In the centrifuge test, different patterns of time histories of the acceleration were observed. The signal was amplified with a ratio of approximately 2.12 from the bottom of the model to the crest of the embankment. The positions under the toes of the embankment had an asymmetrical acceleration profile due to the irregular

geometry of the model above those positions. For the positions under the free ground surface, the liquefaction initiation was observed after two cycles of loading.

- The soil liquefaction was confirmed by the excess pore pressures and the stress paths at various positions in the model. For the positions under the embankment with high confining pressure where liquefaction did not occur, a limited excess pore pressure ratio was observed (around 0.5) and the stress path stabilized before complete liquefaction occurred. For the position at a depth less than 6 m under the ground surface where the soil liquefied, There was a significant increase in excess pore pressure after two cycles, accompanied by a notable decrease in vertical effective stress.
- Soil liquefaction resulted in a soft ground that allowed the embankment to slide approximately as a rigid block. A settlement of 0.7 m was observed at the crest of the embankment, along with a 0.2 m settlement at the middle slope. Furthermore, a heaving of 0.04 m was observed at ground surface level near the toes, indicating a possible lateral spreading of the toes embankment.
- The performance of the numerical model was verified by comparing the acceleration, excess pore pressures and deformations against the experimental results. The numerical model provided reasonable simulation for liquefaction and deformation responses. The symmetrical responses under the embankment and the asymmetrical responses under the toes of the embankment were well captured. Furthermore, the numerical model accurately simulated the attenuation of acceleration near the ground surface after two cycles. Additionally, the build-up of the excess pore pressure was also well reproduced by the numerical model. The deformation trends of the embankment were reflected in the numerical model, which were characterized by settlement at the embankment level and heaving at the free ground surface.
- The boundary effects were analyzed using two new numerical models: an extended model (with over 150m on each side) and a model with free field conditions. Regarding the results, the results from the centrifuge test slightly differ from those from the extended model and the model with free-field conditions. This indicates that the boundaries of the rigid container do not have significant impacts on the responses of the centrifuge model. Based on the numerical results, a zone can be defined in which the behavior of the soil is slightly affected by the numerical boundaries in the original model.

#### **CRediT author statement**

**Chedid SAADE:** Experiment execution, Numerical modeling execution, Data Analysis, Writing- Original draft preparation. **Zheng LI:** Conceptualization, Co-supervision, Investigation, Reviewing and Editing. **Sandra ES-COFFIER:** Conceptualization, Co-supervision, Investigation, Reviewing and Editing. **Luc THOREL:** Conceptualization, Supervision, Investigation, Reviewing and Editing.

507 **Declaration of competing interest**

508 The authors declare no conflict of interest.

509 **Data availability statement**

510 The experimental data presented in the study are available upon direct request to the authors.

511 **Acknowledgment**

512 The financial support of University Gustave Eiffel - Nantes Campus (ex. IFSTTAR) and of the Région Pays de  
513 la Loire is gratefully acknowledged as well as the technical supports from the French National Project – ISOLATE  
514 (Characterizing and Improving SOiLs Against liquEfaction, Grant NO. ANR-17-CE22-0009). The authors would  
515 like also to thank the valuable support and help of the technical staff of the GERS-CG centrifuge lab. Many thanks  
516 to the kind help from Dr. Bogdan Muresan Paslaru and Mme. Laurence Lumiere at Laboratoire EASE, Département  
517 AME, Université Gustave Eiffel Campus de Nantes. The authors would also like to acknowledge all the valuable  
518 comments, suggestions and efforts devoted by the anonymous reviewers to improve the quality of this work.

## References

- Adalier, K., Elgamal, A.W., Martin, G.R., Martin, G.R., 1998. Foundation liquefaction countermeasure for earthquake embankments. *Journal of Geotechnical and Geoenvironmental Engineering*, ASCE 124, 500–517. doi:10.1061/(ASCE)1090-0241(1998)124:6(500).
- Adalier, K., Sharp, M.K., 2004. Embankment dam on liquefiable foundation dynamic behavior and densification remediation. *Journal of Geotechnical and Geoenvironmental Engineering* 130, 1214–1224. doi:10.1061/(ASCE)1090-0241(2004)130:11(1214).
- Adamidis, O., Madabhushi, G.S.P., 2015. Use of viscous pore fluids in dynamic centrifuge modelling. *International Journal of Physical Modelling in Geotechnics* 15, 141–149. doi:10.1680/jphmg.14.00022.
- Adapa, G., Ueda, K., Uzuoka, R., Uzuoka, R., 2021. Seismic stability of embankments with different densities and upstream conditions related to the water level. *Soils and Foundations* 61, 185–197. doi:10.1016/j.sandf.2020.11.007.
- Anderson, J.G., 2004. Quantitative measure of the goodness-of-fit of synthetic seismograms, in: 13th World Conference on Earthquake Engineering, Vancouver, BC, Canada. p. 243.
- Aydingun, O., Adalier, K., 2003. Numerical analysis of seismically induced liquefaction in earth embankment foundations. Part I. Benchmark model. *Canadian Geotechnical Journal* 40, 753–765. doi:10.1139/t03-025.
- Azeiteiro, R.N., Coelho, P.A.L.F., Taborda, D.M.G., Grazina, J.C.D., 2017. Critical state–Based interpretation of the monotonic behavior of Hostun Sand. *Journal of Geotechnical and Geoenvironmental Engineering* 143, 04017004. doi:10.1061/(asce)gt.1943-5606.0001659.
- Basu, D., Montgomery, J., Stuedlein, A.W., 2022. Observations and challenges in simulating post-liquefaction settlements from centrifuge and shake table tests. *Soil Dynamics and Earthquake Engineering* 153, 107089. doi:10.1016/j.soildyn.2021.107089.
- Beaty, M.H., Byrne, P.M., 2011. UBCSAND Constitutive Model: Version 904aR. Technical Report. Itasca.
- Benahmed, N., 2001. Comportement mécanique d'un sable sous cisaillement monotone et cyclique: Application aux phénomènes de liquéfaction et de mobilité cyclique. Ph.D. thesis. Ecole National des Ponts et Chaussées. URL: <http://www.theses.fr/2001ENPC0108>.
- Benahmed, N., Canou, J., Dupla, J.C., 2004. Initial structure and static liquefaction properties of sand. *Comptes Rendus Mécanique* 332, 887–894. doi:10.1016/j.crme.2004.07.009.
- Bhatnagar, S., Kumari, S., Sawant, V.A., Sawant, V.A., 2016. Numerical analysis of earth embankment resting on liquefiable soil and remedial measures. *International Journal of Geomechanics* 16, 04015029. doi:10.1061/(asce)gm.1943-5622.0000501.
- Boulanger, R.W., Montgomery, J., 2016. Nonlinear deformation analyses of an embankment dam on a spatially variable liquefiable deposit. *Soil Dynamics and Earthquake Engineering* 91, 222–233. doi:10.1016/j.soildyn.2016.07.027.
- Boulanger, R.W., Montgomery, J., Ziotopoulou, K., 2015. Nonlinear deformation analyses of liquefaction effects on embankment dams. *Perspectives on Earthquake Geotechnical Engineering, Geotechnical, Geological and earthquake engineering* 37, 247–283. doi:10.1007/978-3-319-10786-8\_10.
- Boulanger, R.W., Ziotopoulou, K., 2015. PM4Sand Version 3 : A sand plasticity model for earthquake engineering applications. Centre for Geotechnical Modeling, University of California .
- Bouraoui, Z., Benmebarek, S., 2018. Modélisation numérique de la déformation induite par la liquéfaction de barrages en terre soumis à des chargements sismiques, in: First International Conference on Dams. ICDBiskra-2018, pp. 479–487.
- Caicedo, B., Thorel, L., 2014. Centrifuge modelling of unsaturated soils. *Journal of Geo-engineering Sciences* 2, pp.83–103. doi:10.3233/JGS-130013.
- Chakraborty, A., Sawant, V.A., 2022. Earthquake response of embankment resting on liquefiable soil with different mitigation models. *Natural Hazards* doi:10.1007/s11069-022-05799-6.
- Chazelas, J.L., Escoffier, S., Garnier, J., Thorel, L., Rault, G., 2008. Original technologies for proven performances for the new LCPC earthquake simulator. *Bulletin of Earthquake Engineering* 6, 723–728. doi:10.1007/s10518-008-9096-z.
- Chen, W.F., Saleeb, A.F., 1994. Constitutive equations for engineering materials. Volume I: Elasticity and modeling. Elsevier Science B.V.
- Chiaradonna, A., Ziotopoulou, K., Carey, T.J., DeJong, J.T., Boulanger, R.W., 2022. Dynamic behavior of uniform clean sands: Evaluation of predictive capabilities in the element- and the system-level scale, in: Geo-Congress 2022, Charlotte, North Carolina. pp. 444–454. doi:10.1061/9780784484043.043.

562 Dafalias, Y.F., Manzari, M.T., 2004. Simple plasticity sand model accounting for fabric change effects. *Journal of engineering mechanics* 130,  
563 622–634. doi:[10.1061/\(ASCE\)0733-9399\(2004\)130:6\(622\)](https://doi.org/10.1061/(ASCE)0733-9399(2004)130:6(622)).

564 Dewoolkar, M.M., Ko, H.Y., Stadler, A.T., Astaneh, S., 1999. A substitute pore fluid for seismic centrifuge modeling. *Geotechnical Testing Journal*  
565 22, 196–210. doi:[10.1520/GTJ11111J](https://doi.org/10.1520/GTJ11111J).

566 Dinesh, N., Banerjee, S., Rajagopal, K., 2022. Performance evaluation of PM4Sand model for simulation of the liquefaction remedial measures  
567 for embankment. *Soil Dynamics and Earthquake Engineering* 152, 107042. doi:[10.1016/j.soildyn.2021.107042](https://doi.org/10.1016/j.soildyn.2021.107042).

568 Doboku, K., 1986. *Manual for Repair Methods of Civil Engineering Structures Damaged by Earthquakes*. vol. 45, Public Works Research Institute,  
569 Ministry of Construction.

570 Duke, C.M., 1960. The chilean earthquakes of May 1960. *Science* 132, 1797–1802. doi:[10.1126/science.132.3442.1797](https://doi.org/10.1126/science.132.3442.1797).

571 Elgamal, A., Parra, E., Yang, Z., Adalier, K., 2002. Numerical analysis of embankment foundation liquefaction countermeasures. *Journal of*  
572 *Earthquake Engineering* 6, 447–471. doi:[10.1080/13632460209350425](https://doi.org/10.1080/13632460209350425).

573 Elgamal, A., Yang, Z., Parra, E., Ragheb, A., 2003. Modeling of cyclic mobility in saturated cohesionless soils. *International Journal of Plasticity*  
574 19, 883–905. doi:[10.1016/S0749-6419\(02\)00010-4](https://doi.org/10.1016/S0749-6419(02)00010-4).

575 Escoffier, S., Audrain, P., 2020. Leap-ucd-2017 centrifuge test at ifsttar, in: Kutter, B.L., Manzari, M.T., Zeghal, M. (Eds.), *Model Tests*  
576 *and Numerical Simulations of Liquefaction and Lateral Spreading*, Springer International Publishing, Cham. pp. 293–313. doi:[10.1007/](https://doi.org/10.1007/978-3-030-22818-7_15)  
577 [978-3-030-22818-7\\_15](https://doi.org/10.1007/978-3-030-22818-7_15).

578 Finn, W.D.L., 1999. Evolution of dynamic analysis in geotechnical earthquake engineering, in: *Workshop on New Approaches to Liquefaction*  
579 *Analysis*, Washington, D.C., United States. pp. 1–18.

580 Garnier, J., 2001. Physical models in geotechnics: state of the art and recent advances, in: *Proceedings of the 1st International Albert Caquot*  
581 *Conference*, Paris, France. pp. 1–51.

582 Garnier, J., Gaudin, C., Springman, S., Culligan, P., Gooding, D., Konig, D., Kutter, B., Phillips, R., Randolph, M., Thorel, L., 2007. Catalogue of  
583 scaling laws and similitude questions in geotechnical centrifuge modelling. *International Journal of Physical Modelling in Geotechnics* 3, 1–23.  
584 doi:[10.1680/ijpimg.2007.070301](https://doi.org/10.1680/ijpimg.2007.070301).

585 Gobbi, S., 2020. Characterization of liquefaction parameters for saturated soil under dynamic loading using laboratory tests and calibration of  
586 constitutive laws by numerical modelling. Ph.D. thesis. Université Paris-Est. URL: <https://theses.hal.science/tel-03268600>.

587 Gobbi, S., Lopez-caballero, F., Forcellini, D., 2017. Numerical analysis of soil liquefaction induced failure of embankments, in: *6th International*  
588 *Conference on Computational Methods in Structural Dynamics and Earthquake Engineering, COMPDYN 2017*, National Technical University  
589 of Athens. pp. 990–1006.

590 Gobbi, S., Reiffsteck, P., Lenti, L., D’Avila, M.P.S., Semblat, J.F., 2022a. Liquefaction triggering in silty sands: effects of non-plastic fines and  
591 mixture-packing conditions. *Acta Geotechnica* 17, 391–410. doi:[10.1007/s11440-021-01262-1](https://doi.org/10.1007/s11440-021-01262-1).

592 Gobbi, S., Santisi d’Avila, M.P., Lenti, L., Semblat, J.F., Reiffsteck, P., 2022b. Liquefaction assessment of silty sands: Experimental characterization  
593 and numerical calibration. *Soil Dynamics and Earthquake Engineering* 159, 107349. doi:[10.1016/j.soildyn.2022.107349](https://doi.org/10.1016/j.soildyn.2022.107349).

594 Higo, Y., Lee, C.W., Doi, T., Kinugawa, T., Kimura, M., Kimoto, S., Oka, F., 2015. Study of dynamic stability of unsaturated embankments with  
595 different water contents by centrifugal model tests. *Soils and Foundations* 55, 112–126. doi:[10.1016/j.sandf.2014.12.009](https://doi.org/10.1016/j.sandf.2014.12.009).

596 Idriss, I., Boulanger, R., 2008. *Soil liquefaction during earthquakes*. Earthquake Engineering Research Institute.

597 Iwasaki, T., 1986. Soil liquefaction studies in japan: state-of-the-art. *Soil Dynamics and Earthquake Engineering* 5, 2–68. doi:[10.1016/](https://doi.org/10.1016/0267-7261(86)90024-2)  
598 [0267-7261\(86\)90024-2](https://doi.org/10.1016/0267-7261(86)90024-2).

599 Izawa, J., Doi, T., Suzuki, A., Kojima, K., 2022. Seismic Design of Embankments in Consideration of Damage Process during Earthquakes.  
600 *Quarterly Report of RTRI* 63. doi:[10.2219/rtriqr.63.1\\_56](https://doi.org/10.2219/rtriqr.63.1_56).

601 Jovičić, V., Coop, M.R., Simić, M., 1996. Objective criteria for determining Gmax from bender element tests. *Géotechnique* 46, 357–362.  
602 doi:[10.1680/geot.1996.46.2.357](https://doi.org/10.1680/geot.1996.46.2.357).

603 Karl, L., Haegeman, W., Degrande, G., Dooms, D., 2008. Determination of the material damping ratio with the bender element test. *Journal of*  
604 *geotechnical and geoenvironmental engineering* 134, 1743–1756. doi:[10.1061/\(ASCE\)1090-0241\(2008\)134:12\(1743\)](https://doi.org/10.1061/(ASCE)1090-0241(2008)134:12(1743)).

- Kassas, K., 2021. Structure-Soil-Structure Interaction (SSSI) of adjacent buildings founded on liquefiable soil. Ph.D. thesis. ETH Zurich. Zurich. doi:[10.3929/ethz-b-000511100](https://doi.org/10.3929/ethz-b-000511100).
- Kassas, K., Adamidis, O., Anastopoulos, I., 2021a. Shallow strip foundations subjected to earthquake-induced soil liquefaction : Validation , modelling uncertainties , and boundary effects. *Soil Dynamics and Earthquake Engineering* 147, 106719. doi:[10.1016/j.soildyn.2021.106719](https://doi.org/10.1016/j.soildyn.2021.106719).
- Kassas, K., Adamidis, O., Gerolymos, N., Anastopoulos, I., 2021b. Numerical modelling of a structure with shallow strip foundation during earthquake-induced liquefaction. *Géotechnique* 71, 1099–1113. doi:[10.1680/jgeot.19.p.277](https://doi.org/10.1680/jgeot.19.p.277).
- Kawakami, F., Asada, A., 1966. Damage to the ground and earth structures by the niigata earthquake of june 16, 1964. *Soils and Foundations* 6, 14–30. doi:[10.3208/sandf1960.6.14](https://doi.org/10.3208/sandf1960.6.14).
- Koga, Y., Matsuo, O., 1990. Shaking table tests of embankments resting on liquefiable sandy ground. *Soils and Foundations* 30, 162–174. doi:[10.3208/sandf1972.30.4\\_162](https://doi.org/10.3208/sandf1972.30.4_162).
- Kumar, J., Shinde, N., 2019. Interpretation of bender element test results using sliding fourier transform method. *Canadian Geotechnical Journal* 56, 2004–2014. doi:[10.1139/cgj-2018-0733](https://doi.org/10.1139/cgj-2018-0733).
- Ladd, R., 1974. Specimen preparation and liquefaction of sands. *Journal of Geotechnical and Geoenvironmental Engineering* 100, 1180–1184. doi:[10.1061/AJGEB6.0000117](https://doi.org/10.1061/AJGEB6.0000117).
- Lee, J., Santamarina, J., 2005. Bender elements: Performance and signal interpretation. *Journal of Geotechnical and Geoenvironmental Engineering* 131, 1063–1070. doi:[10.1061/\(asce\)1090-0241\(2005\)131:9\(1063\)](https://doi.org/10.1061/(asce)1090-0241(2005)131:9(1063)).
- Li, Y., Kitazume, M., Takahashi, A., Harada, K., Ohbayashi, J., 2021. Centrifuge study on the effect of the SCP improvement geometry on the mitigation of liquefaction-induced embankment settlement. *Soil Dynamics and Earthquake Engineering* 148, 106852. doi:[10.1016/j.soildyn.2021.106852](https://doi.org/10.1016/j.soildyn.2021.106852).
- Li, Z., Escoffier, S., Kotronis, P., 2013. Using centrifuge tests data to identify the dynamic soil properties: Application to Fontainebleau sand. *Soil Dynamics and Earthquake Engineering* 52, 77–87. doi:[10.1016/j.soildyn.2013.05.004](https://doi.org/10.1016/j.soildyn.2013.05.004).
- Lu, C.C., Chen, K.Y., Cheng, Y.T., Han, Y.H., 2022. Seismic Performance Screening and Evaluation for Embankments on Liquefiable Foundation Soils. *Geosciences* 12, 1–25. doi:[10.3390/geosciences12060221](https://doi.org/10.3390/geosciences12060221).
- Mazzoni, S., McKenna, F., Scott, M.H., Fenves, G.L., 2006. OpenSees command language manual. Pacific Earthquake Engineering Research (PEER) Center, University of California, Berkeley URL: <http://opensees.berkeley.edu/manuals/usermanual>.
- McGann, C.R., Arduino, P., Mackenzie-Helnwein, P., 2012. Stabilized single-point 4-node quadrilateral element for dynamic analysis of fluid saturated porous media. *Acta Geotechnica* 7, 297–311. doi:[10.1007/s11440-012-0168-5](https://doi.org/10.1007/s11440-012-0168-5).
- McKenna, F., Mazzoni, S., Scott, M.H., Fenves, G.L., 2006. OpenSees command language manual. University of California, Berkeley, CA.
- Mulilis, J.P., 1975. The effects of method of sample preparation on the cyclic stress-strain behaviour of sands. Technical Report, Univ. of California at Berkeley 75.
- Mulilis, J.P., Seed, H.B., Chan, C.K., Mitchell, J.K., Arulanandan, K., 1977. Effects of sample preparation on sand liquefaction. *Journal of the Geotechnical Engineering Division* 103, 91–108. doi:[10.1061/AJGEB6.0000387](https://doi.org/10.1061/AJGEB6.0000387).
- Murillo, C., Sharifpour, M., Caicedo, B., Thorel, L., Dano, C., 2011. Elastic parameters of intermediate soils based on bender-extender elements pulse tests. *Soils and Foundations* 51, 637–649. doi:[10.3208/sandf.51.637](https://doi.org/10.3208/sandf.51.637).
- Ng, C.W., Li, X.S., Van Laak, P.A., Hou, D.Y., 2004. Centrifuge modeling of loose fill embankment subjected to uni-axial and bi-axial earthquakes. *Soil Dynamics and Earthquake Engineering* 24, 305–318. doi:[10.1016/j.soildyn.2003.12.002](https://doi.org/10.1016/j.soildyn.2003.12.002).
- Oblak, A., Kosic, M., Viana Da Fonseca, A., Logar, J., 2020. Fragility Assessment of Traffic Embankments Exposed to Earthquake-Induced Liquefaction. *Applied sciences* doi:[10.3390/app10196832](https://doi.org/10.3390/app10196832).
- Oka, F., Tsai, P., Kimoto, S., Kato, R., 2012. Damage patterns of river embankments due to the 2011 off the pacific coast of tohoku earthquake and a numerical modeling of the deformation of river embankments with a clayey subsoil layer. *Soils and Foundations* 52, 890–909. doi:[10.1016/j.sandf.2012.11.010](https://doi.org/10.1016/j.sandf.2012.11.010).
- Okamura, M., Inoue, T., 2012. Preparation of fully saturated models for liquefaction study. *International Journal of Physical Modelling in*



Geotechnics 12, 39–46. doi:10.1680/ijpmpg.2012.12.1.39.

Okamura, M., Matsuo, O., 2002. Effects of remedial measures for mitigating embankment settlement due to foundation liquefaction. *International Journal of Physical Modelling in Geotechnics* 2, 01–12. doi:10.1680/ijpmpg.2002.020201.

Okamura, M., Tamamura, S., Yamamoto, R., 2013. Seismic stability of embankments subjected to pre-deformation due to foundation consolidation. *Soils and Foundations* 53, 11–22. doi:10.1016/j.sandf.2012.07.015.

Okochi, Y., Sreng, S., Matsumoto, M., Miki, H., Tsuda, M., Ito, H., 2015. Dynamic centrifuge model tests of embankment with a new liquefaction countermeasure by ground improvement considering constraint effect, in: 6th International Conference on Earthquake Geotechnical Engineering, Christchurch, New Zealand Numerical. pp. 1–10.

OpenSees, 2020. OpenSees – Open System for Earthquake Engineering Simulation. <https://opensees.berkeley.edu/>. Version 3.2.2 released on July 3, 2020.

Park, Y.H., Kim, S.R., Kim, S.H., Kim, M.M., 2000. Liquefaction of embankments on sandy soils and the optimum countermeasure against the liquefaction. *Journal of the Korean Geotechnical Society* 16, 15–21.

Pourakbar, M., Khosravi, M., Soroush, A., Hung, W.Y., Hoang, K.K., Nabizadeh, A., 2022. Dynamic centrifuge tests to evaluate the seismic performance of an embankment resting on liquefiable ground improved by unreinforced and reinforced soil-cement columns. *Journal of Geotechnical and Geoenvironmental Engineering* 148, 04022106. doi:10.1061/(ASCE)GT.1943-5606.0002891.

Pramaditya, A., Fathani, T., 2021a. Physical modelling of earthquake-induced liquefaction on uniform soil deposit and settlement of earth structures. *Journal of the Civil Engineering Forum* 7, 85–96. doi:10.22146/jcef.59467.

Pramaditya, A., Fathani, T.F., 2021b. Geotechnical centrifuge test of reinforced road embankment against earthquake-induced liquefaction. *International Journal of GEOMATE* 21, 115–122. doi:10.21660/2021.85.j2256.

Rahmani, A., Ghasemi Fare, O., Pak, A., 2012. Investigation of the influence of permeability coefficient on the numerical modeling of the liquefaction phenomenon. *Scientia Iranica* 19, 179–187. doi:10.1016/j.scient.2012.02.010.

Rapti, I., Lopez-Caballero, F., Modaressi-Farahmand-Razavi, A., Foucault, A., Voldoire, F., 2018. Liquefaction analysis and damage evaluation of embankment-type structures. *Acta Geotechnica* 13, 1041–1059. doi:10.1007/s11440-018-0631-z.

Saade, C., Li, Z., Escoffier, S., Thorel, L., 2022. Etude des effets de bord dans les essais centrifuges sous chargement sismique par modélisation numérique, in: 11èmes journées nationales de géotechnique et de géologie de l'ingénieur, Institut National des Sciences Appliquées de Lyon [INSA Lyon], CFMS, CFMR, CFGI, Lyon, France. pp. 1–8.

Santisi d'Avila, M.P., Semblat, J.F., 2014. Nonlinear seismic response for the 2011 Tohoku earthquake: borehole records versus 1 Directional - 3 Component propagation models. *Geophysical Journal International* , 1–15. doi:10.1093/gji/ggu004.

Seed, H.B., Lee, K.L., Idriss, I.M., Makdisi, F.I., 1975. The slides in the san fernando dams during the earthquake of february 9, 1971. *Journal of the Geotechnical Engineering Division* 101, 651–688. doi:10.1061/AJGEB6.0000178.

Seed, H.B., Makdisi, F.I., De Alba, P., De Alba, P., 1980. Performance of earth dams during earthquakes. *International Water Power and Dam Construction* 32, 17–27. doi:10.1061/AJGEB6.0000675.

Seth, D., Manna, B., Shahu, J.T., Fazeres-Ferradosa, T., Figueiredo, R., Romão, X., Rosa-Santos, P., Taveira-Pinto, F., 2022. Numerical modelling of the effects of liquefaction on the upheaval buckling of offshore pipelines using the PM4Sand model. *Energies* 15, 5561. doi:10.3390/en15155561.

Shahbodagh, B., Sadeghi, H., Kimoto, S., Oka, F., 2020. Large deformation and failure analysis of river embankments subjected to seismic loading. *Acta Geotechnica* 15, 1381–1408. doi:10.1007/s11440-019-00861-3.

Shahir, H., Mohammadi-Haji, B., Ghassemi, A., 2014. Employing a variable permeability model in numerical simulation of saturated sand behavior under earthquake loading. *Computers and Geotechnics* 55, 211–223. doi:10.1016/j.compgeo.2013.09.007.

Shahir, H., Pak, A., Taiebat, M., Jeremić, B., 2012. Evaluation of variation of permeability in liquefiable soil under earthquake loading. *Computers and Geotechnics* 40, 74–88. doi:10.1016/j.compgeo.2011.10.003.

Sze, H.Y., Yang, J., 2014. Failure Modes of Sand in Undrained Cyclic Loading : Impact of Sample Preparation. *Journal of Geotechnical and Geoenvironmental Engineering* 140, 152–169. doi:10.1061/(ASCE)GT.1943-5606.0000971.



691 Tatsuoka, F., Ochi, K., Fujii, S., Okamoto, M., 1986. Cyclic undrained triaxial and torsional shear strength of sands for different sample preparation  
692 methods. *Soils and Foundations* 26, 23–41. doi:[10.3208/sandf1972.26.3\\_23](https://doi.org/10.3208/sandf1972.26.3_23).

693 Tiznado, J.C., Dashti, S., Ledezma, C., Wham, B.P., Badanagki, M., 2020. Performance of embankments on liquefiable soils improved with dense  
694 granular columns: Observations from case histories and centrifuge experiments. *Journal of Geotechnical and Geoenvironmental Engineering*  
695 146, 04020073. doi:[10.1061/\(ASCE\)GT.1943-5606.0002309](https://doi.org/10.1061/(ASCE)GT.1943-5606.0002309).

696 Tobita, T., 2020. Variation of permeability of viscous fluid during liquefaction model testing, in: Kutter, B.L., Manzari, M.T., Zeghal, M. (Eds.),  
697 Model Tests and Numerical Simulations of Liquefaction and Lateral Spreading, Springer International Publishing, Cham. pp. 649–652. doi:[10.1007/978-3-030-22818-7\\_37](https://doi.org/10.1007/978-3-030-22818-7_37).

698 Ueno, K., 1998. Methods for preparation of sand samples, in: Kimura, Balkema, T. (Eds.), *Proceedings of the International Conference Centrifuge*,  
699 Tokyo. pp. 1047–1056.

700 USSD, 2022. Analysis of Seismic Deformations of Embankment Dams. Technical Report. United States Society on Dams. URL: [www.ussdams.org](http://www.ussdams.org).

701  
702 [org](http://www.ussdams.org).

703 Veylon, G., 2017. Modélisation numérique du mécanisme de liquéfaction des sols : application aux ouvrages hydrauliques. Ph.D. thesis. Université  
704 Grenoble Alpes. URL: <http://www.theses.fr/2017GREAI019>.

705 Wang, Z., Ma, F., 2019. Bounding surface plasticity model for liquefaction of sand with various densities and initial stress conditions. *Soil*  
706 *Dynamics and Earthquake Engineering* 127, 105843. doi:[10.1016/j.soildyn.2019.105843](https://doi.org/10.1016/j.soildyn.2019.105843).

707 Wu, C., Ni, C., Ko, H., 2009. Seismic response of an earth dam: finite element coupling analysis and validation from centrifuge tests. *Journal of*  
708 *Rock Mechanics and Geotechnical Engineering* 1, 56–70. doi:[10.3724/sp.j.1235.2009.00056](https://doi.org/10.3724/sp.j.1235.2009.00056).

709 Wu, W., Berhe, T., Ashour, T., 2012. 20 - embankments and dams, in: Hall, Lindsay, Krayenhoff (Eds.), *Modern Earth Buildings*. Woodhead  
710 Publishing Series in Energy, pp. 538–558. doi:[10.1533/9780857096166.4.538](https://doi.org/10.1533/9780857096166.4.538).

711 Yamaguchi, A., Mori, T., Kazama, M., Yoshida, N., Yoshida, N., 2012. Liquefaction in Tohoku district during the 2011 off the Pacific Coast of  
712 Tohoku Earthquake. *Soils and Foundations* 52, 811–829. doi:[10.1016/j.sandf.2012.11.005](https://doi.org/10.1016/j.sandf.2012.11.005).

713 Zeghal, M., Elgamal, A.W., 1994. Analysis of site liquefaction using earthquake records. *Journal of Geotechnical Engineering* 120, 996–1017.  
714 doi:[10.1061/\(ASCE\)0733-9410\(1994\)120:6\(996\)](https://doi.org/10.1061/(ASCE)0733-9410(1994)120:6(996)).

715 Ziotopoulou, K., 2018. Seismic response of liquefiable sloping ground: Class a and c numerical predictions of centrifuge model responses. *Soil*  
716 *Dynamics and Earthquake Engineering* 113, 744–757. doi:[10.1016/j.soildyn.2017.01.038](https://doi.org/10.1016/j.soildyn.2017.01.038).